Contrib Mineral Petrol (2007) 153:509–531
DOI 10.1007/s00410-006-0164-6

ORIGINAL PAPER

Simultaneous boninitic and arc-tholeiitic volcanisms in the Izu forearc region during early arc volcanism, based on ODP Leg 125 Site 786

Satoru Haraguchi · Teruaki Ishii

Received: 29 April 2006 / Accepted: 13 October 2006 / Published online: 6 January 2007

Abstract Early arc volcanism during Eocene to Oligocene in the Izu forearc region was investigated during ODP Legs 125 and 126 in 1989, and effusive and intrusive volcanics were recovered from Leg 125 Site 786. These rocks were all classified into boninites and associated rocks by Leg 125 Shipboard Scientific Party, and they concluded that boninitic volcanism had occurred before 40 Ma, and arc tholeiitic volcanism began after 40 Ma. In this study, lava flows and breccias that classified into boninite series are divided into two groups, tholeiite and boninite, based on petrographical and petrological properties. Both series are also distinguished by bulk rock composition. It is considered that the sources of both rock types have similar depleted compositions because of their similar, very low bulk HFSE concentrations. We suggest that boninitic and tholeiitic volcanism occurred closely in time and space, and reflected different temperature and water condition.

Keywords Boninite · Tholeiite · Early arc volcanism · Two-pyroxene geothermometry · Water condition

Introduction

The Philippine Sea region is characterized by the Izu-Ogasawara (Bonin)-Mariana (IBM) active arc, the Kyushu-Palau Ridge, with the Shikoku Basin intervening between these geographic highs, and the West Philippine Basin existing west side of the latter ridge (Fig. 1a). These volcanic terranes comprise the back-arc basin that was formed as a result of the westward subduction of the Pacific Plate beneath the Philippine Sea Plate (e.g., Honza and Fujioka 2004). Arc volcanism in the proto-IBM arc, which was active before the Shikoku Basin opened, is characterized by boninite series magmatism succeeded by tholeiite and calc-alkaline series magmatism. Boninite is one of the characteristics of early arc volcanism (e.g., Tatsumi and Maruyama 1989), and this volcanism censed in the IBM arc during middle to late Eocene (e.g., Taylor et al. 1994).

The Izu forearc region was investigated during Ocean Drilling Program (ODP) Legs 125 and 126. ODP Leg 125 Site 786 (31°52.5′N, 141°13.6′E) is located about 130 km east of Myojin-Sho Island (Fig. 1b), the closest active subaerial volcano of the IBM arc, in the Izu outer-arc high which is probably made up as submarine volcanic edifices during the time of the Eocene to early Oligocene. Arculus et al. (1992) classified recovered volcanic rocks based on bulk rock chemistry, and they concluded that these are made up of basic to acidic rocks of the boninite series. Mitchell et al. (1992) investigated radiometric K–Ar dating of these rocks and concluded that the age of effusive rocks (flow and breccia) is 41.3 ± 0.5 Ma and that of later stage dikes or sills show two stages, 34.6 ± 0.7 and 17 Ma. However, Ar–Ar dates of the same rocks are older than the K–Ar ages, about 47–45 Ma, and the younger pulse dated at 35 Ma by K–Ar method is obscured (Cosca et al. 1998; Fig. 2).

The processes and rock types associated with early stages in the volcanic evolution of island arcs are not

---

Communicated by T. L. Grove.

S. Haraguchi (✉) · T. Ishii
Ocean Research Institute, University of Tokyo,
Nakano 164-8639, Japan
e-mail: haraguti@ori.u-tokyo.ac.jp

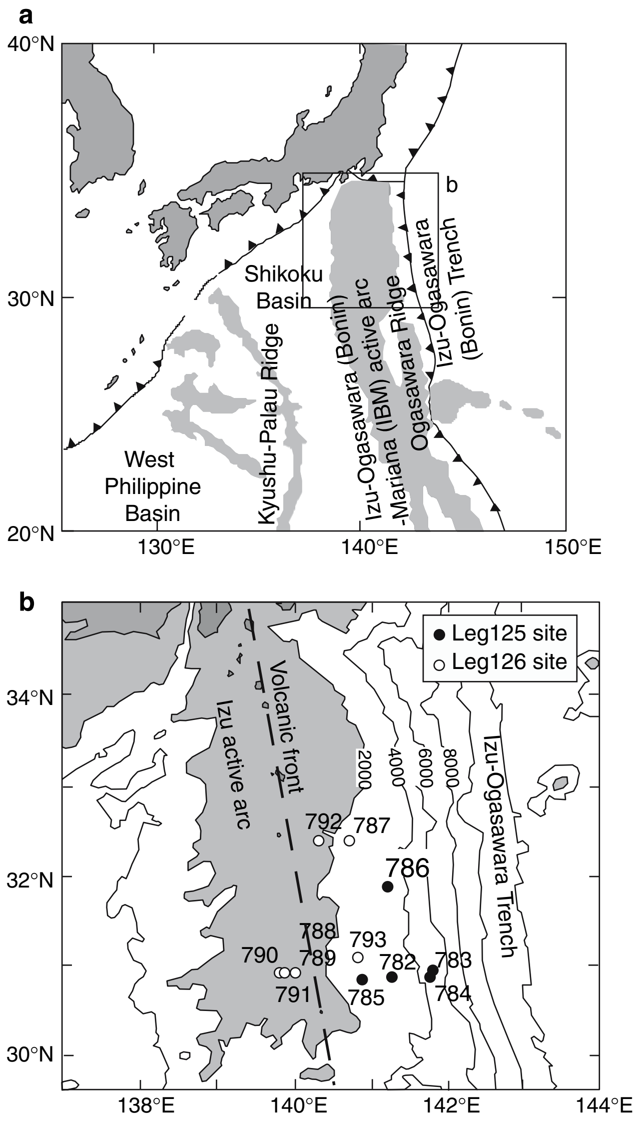

Fig. 1 **a** Location map of the Philippine Sea region and Japan. **b** Bathymetry of the northern Izu are region, and drill sites from Legs 125 (*solid circules*) and 126 (*open circles*)

well understood. One of the reasons is that the products of these stages are generally deeply buried beneath eruptions that are more recent. However, recent drilling and dredging of island arcs in the Philippine Sea Plate have provided important new data that bear on this problem.

Methods

Site 786 samples used in this study were selected from the stored rocks in the ODP head office, Texas A&M University. Samples are mainly selected from the same rock pieces having known bulk compositions measured by Arculus et al. (1992) and Murton et al. (1992). Thin sections were made from the chosen 201 rock pieces, and mineral compositions were estimated by the electron probe micro analyzer (EPMA), on the representative 47 effusive rock samples (Table 1).

Mineral phases were analyzed by JEOL-733 electron microprobe at the Ocean Research Institute, University of Tokyo, using 15 KV accelerating potential, 1.2×10^{-8} A sample current, 1 μm beam, natural and systematic mineral standards, and the correlation factors of Bence and Albee (1968). Alpha factor is based on Nakamura and Kushiro (1970). Thirteen elements were analyzed: SiO_2, TiO_2, Al_2O_3, FeO, MnO, MgO, CaO, Na_2O, K_2O, Cr_2O_3, V_2O_3, NiO, and P_2O_5. Five or Ten analytical points were selected along a straight line from core to rim for both phenocrysts and microphenocrysts. Two points were analyzed for core and rim of groundmass minerals. About 300–500 points were chosen for each thin section and were recorded in photomicrographs.

Petrography

Arculus et al. (1992) divided volcanic basement from Site 786 into 34 subunits based on lithological contrasts and geochemical characteristics. Generally, effusive rocks are phanerocrystalline porphyritic with glassy groundmass. However, intrusive rocks have rare phenocrysts bearing many groundmass minerals. These volcanic rocks were classified into boninite series based on TiO_2, Y contents and Pb isotope data (Arculus et al. 1992; Murton et al. 1992; Pearce et al. 1992a).

Effusive rocks, flows and volcanic breccias are divided into two groups based on textures and mineral assemblages. One group is characterized by low mode and small size of phenocrysts mainly plagioclase (pl) and glassy groundmass. This group is called ‘Type A’ in this study (Fig. 3a, b). The other group is characterized by high mode and larger sizes of phenocrysts mainly orthopyroxene (opx) and clinopyroxene (cpx), and relatively non-glassy groundmass. This group is called ‘Type B’ in this study (Fig. 3c, d).

Type A samples

The Type A rocks show aphyric or porphyritic texture, the latter contains less than 10% of phenocrysts. Phenocrysts are mainly opx, cpx, pl and a minor amount of magnetite (mt), the first three occurs in a ratio of 1:2:3 with plagioclase occupying about half of the total volume of phenocrysts. However, certain amount of phenocrysts decrease with increase of SiO_2 content in bulk composition and volcanic glass in groundmass.

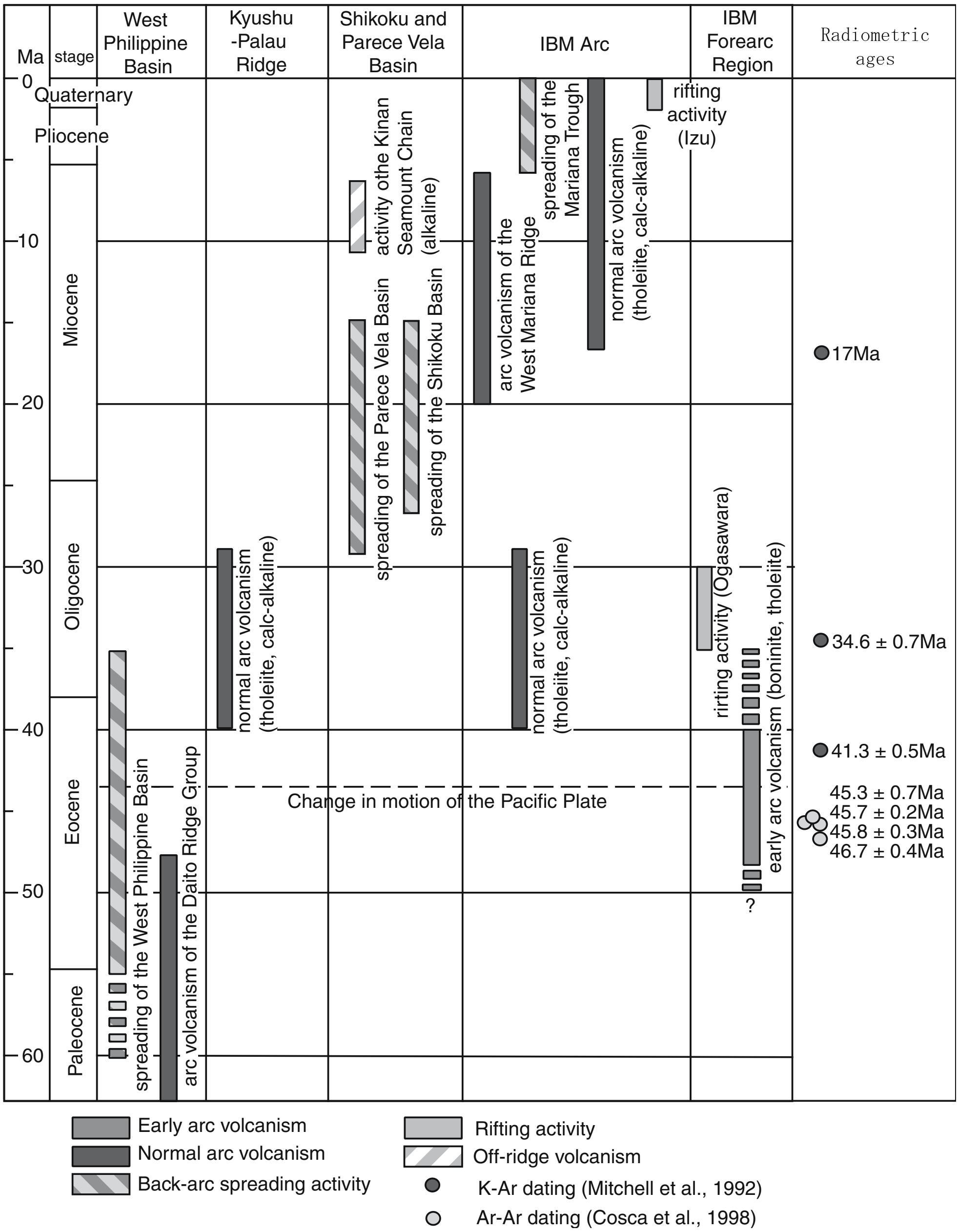

Fig. 2 Space–time distribution of volcanic activity in the Philippine Sea Plate (modified Haraguchi et al. 2003), including radiometric K–Ar ages (Mitchell et al. 1992; *filled circles*) and Ar–Ar ages (Cosca et al. 1998; *open circles*) of Site 786 rocks

Pl phenocrysts are euhedral to subhedral, up to 1 mm long. The minerals shows short to long prismatic shape, low relief, and commonly have lamellar twins, not observed complex zoning patterns and glass inclusion is rarely observed. Opx phenocrysts are one-third of the amount of pl. They are euhedral to subhedral, fine to coarse (up to 2 mm long) grained prismatic shape. They show columnar or lath-shaped and slightly brownish in plane-polarized light. Reverse zoning is not observed under the cross nicol. Cpx phenocrysts are two times the amount of opx. They are euhedral to subhedral, fine to coarse (up to 2 mm long) grained prismatic shape. They show faintly greenish color in plane-polarized light, high birefringence and oblique extinction. They are commonly twinned, and one set of cleavage planes is usually prominent. Reverse zoning is not observed under the cross nicol similar to that of the opx. Groundmass minerals are mostly pl, and minor amounts of pyroxene. Groundmass glasses show dark gray to black color under open nicol. Pl in the groundmass has a columnar to acicular shape, low relief, and most of the groundmass mineral has twinning. Small amounts of euhedral to anhedral mt are commonly found as the opaque phase in the

Table 1 Description of the EPMA-analyzed samples at ODP Leg 125 Site 786

Unit	Upper (cm)	Lower (cm)	Depth (mbsf)	Volume (cc)	Rock type (Arculus et al. 1992)	Lith. unit	Rock series (This study)
786B-1R-1	46	49	163	7	ICBrzA Flow	1	Type B
786B-1R-1	88	92	163.4	7	ICBrzA Flow	1	Type B
786B-2R-1	88	91	170.4	5	ICBrzA Flow	1	Type B
786B-3R-1	90	94	180.1	10	ICBrzA Flow	1	Type B
786B-5R-1	10	14	198.7	5	ICBrzA Flow	1	Type B
786B-5R-1	107	111	199.7	7	ICBrzA Flow	1	Type B
786B-5R-2	10	13	200.2	5	ICBrzA Flow	1	Type B
786B-5R-2	32	36	200.4	7	ICBrzA Flow	1	Type B
786B-8R-1	40	42	228	10	A Breccia	3	Type A
786B-9R-1	11	17	237.2	10	A Breccia	3	Type A
786B-9R-1	25	30	237.4	15	A Breccia	3	Type A
786B-11R-1	120	122	257.1	8	ICB/BrzA Breccia	4	Type B
786B-12R-2	59	64	268	6	ICB/BrzA Breccia	4	Type B
786B-12R-2	123	127	268.7	6	ICB/BrzA Breccia	4	Type B
786B-13R-2	18	21	277.3	6	ICB/BrzA Breccia	4	Type B
786B-13R-2	133	136	278.5	5	ICB/BrzA Breccia	4	Type B
786B-15R-2	85	88	297.3	6	A Breccia	5	Type A
786B-16R-2	81	85	306.9	5	A Breccia	5	Type A
786B-17R-1	60	63	314.9	6	A Breccia	5	Type A
786B-18R-1	57	60	324.5	4	A Flow	6	Type A
786B-21R-1	22	26	353.2	7	A Flow	6	Type A
786B-21R-1	120	122	354.2	5	R Flow	8	Type A
786B-21R-1	135	138	354.4	4	R Flow	8	Type A
786B-24R-1	136	140	383.3	5	D Flow	11	Type A
786B-25R-1	63	67	392.1	7	D Flow	11	Type A
786B-26R-1	97	102	402.2	10	D Flow	11	Type A
786B-27R-1	91	94	411.7	5	D Breccia	11	Type A
786B-28R-1	14	18	420.5	9	ICBrzA Breccia	13	Type B
786B-29R-1	69	73	430.8	8	ICBrzA Breccia	13	Type B
786B-30R-1	1	5	439.7	10	ICBrzA Breccia	13	Type B
786B-31R-1	108	110	450.5	6	ICBrzA Breccia	13	Type B
786B-32R-1	57	61	459.6	10	ICBrzA Breccia	13	Type B
786B-32R-2	82	85	461.3	6	R Flow	16	Type A
786B-35R-1	132	137	489.3	15	D–R Flow	20	Type B
786B-35R-2	2	5	489.5	9	D–R Flow	20	Type B
786B-35R-2	87	91	490.4	8	D–R Flow	20	Type B
786B-36R-1	52	56	498.2	8	D–R Flow	20	Type B
786B-38R-1	74	78	517.8	12	A Flow	22	Type A
786B-39R-1	49	52	527.3	8	A Flow	22	Type A
786B-39R-2	118	122	529.5	12	A Flow	22	Type A
786B-42R-2	11	16	557.3	10	ICBrzA Flow	24	Type B
786B-43R-2	88	91	567.2	7	ICBrzA Flow	24	Type B
786B-45R-1	24	27	584.5	7	ICBrzA Breccia	24	Type B
786B-45R-1	46	50	584.8	7	ICBrzA Breccia	24	Type B
786B-49R-4	33	36	627	5	ICBrzA Breccia	24	Type B
786B-49R-4	54	57	627.2	11	ICBrzA Breccia	24	Type B
786B-51R-1	53	37	642.7	9	ICB/BrzA Breccia	26	Type B

groundmass or as microphenocrysts with size up to 0.5 mm are common in some samples.

Type B samples

The Type B rocks are more porphyritic than the Type A rocks and contain 10–30% of phenocrysts. Phenocrysts are mainly opx, cpx and pl. The ratio of opx, cpx and pl in the most primitive rocks is about 2:2:1. Quantities of opx and cpx phenocrysts are decreasing and that of pl phenocrysts are increasing with growing bulk SiO_2 content. In general, total amount of phenocrysts decreases with increasing SiO_2 content.

Opx phenocrysts are the most common mineral in the Type B rocks. They are euhedral to subhedral, fine to coarse (up to 2 mm long) grained prismatic shape. The mineral is columnar or lath-shaped and slightly brownish in plane-polarized light. Reverse zoning is observed in some phenocrysts under the cross nicol. The amount of cpx phenocrysts is about half of opx.

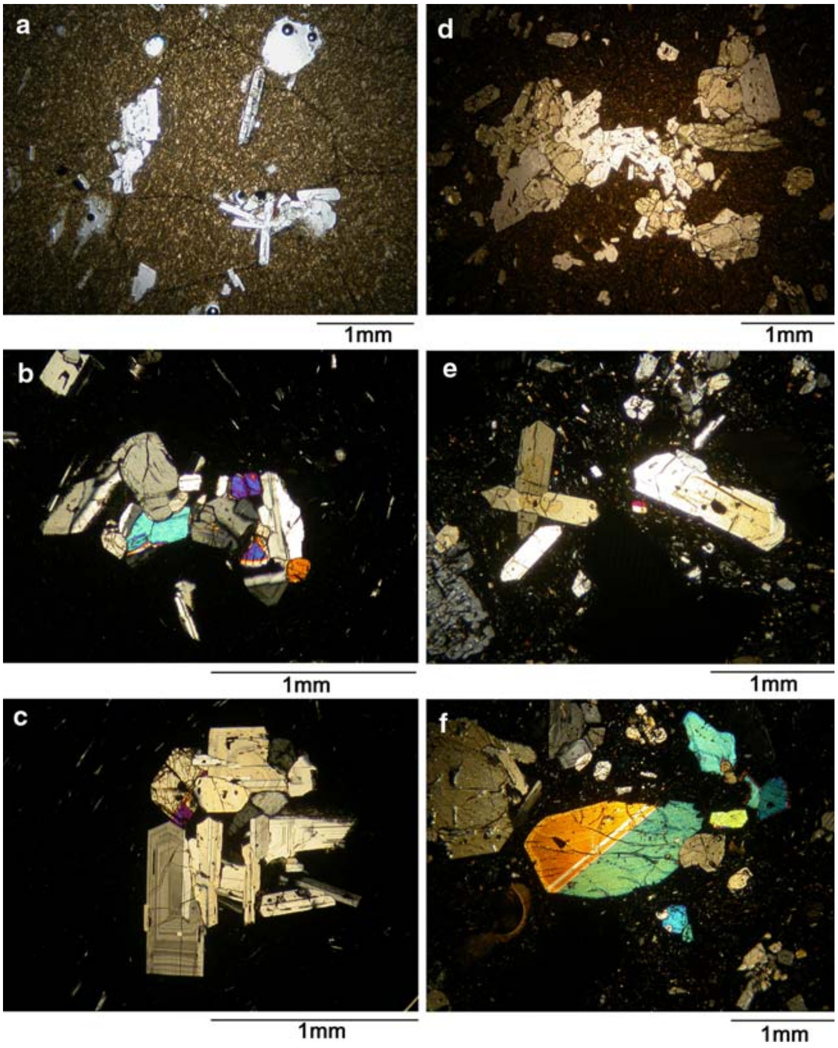

Fig. 3 **a** Plagioclase phenocrysts (*left*), clinopyroxene phenocryst (*right above*) and glomeroporphyritic texture composed of clinopyroxene and plagioclase microphenocrysts (*right under*) in the typical Type A sample (786B-16R-2, 81–85 cm, 306.88 mbsf, Unit 5). Plane-polarized light. **b** Glomeroporphyritic texture mainly composed of two-pyroxene and plagioclase in the other Type A sample (786B-9R-1, 11–17 cm, 237.21 mbsf, Unit 3). Crossed polars. **c** Glomerophyric texture composed of plagioclase in the same Type A sample of **b**. Compositional zoning are observed in these pl phenocrysts. Crossed polars. **d** Glomeroporphyritic texture composed of two-pyroxene and plagioclase phenocrysts in the Type B sample (786B-45R-1, 46–50 cm, 584.76 mbsf, Unit 24). Plane-polarized light. **e** Orthopyroxene phenocrysts in the typical Type B sample (786B-51R-1, 53–57 cm, 642.73 mbsf, Unit 26). Reverse zoning are observed in these opx phenocrysts. Crossed polars. **f** Clinopyroxene phenocrysts in the same Type B sample of **e**. The center cpx phenocryst shows reverse zoning and twinning. Crossed polars

They are euhedral to subhedral, fine to coarse (up to 2 mm long) grained prismatic shape. The mineral is columnar or lath-shaped, faintly greenish in plane-polarized light and exhibit high birefringence and oblique extinction. Crystals are commonly twinned, and one set of cleavage planes is usually prominent. A reverse zoning is observed in some phenocrysts under the cross nicol similar to that of the opx. The amount of pl phenocrysts is about half of opx. They are euhedral to subhedral, fine to large (up to 2 mm long) grained prismatic shape. They show columnar or lath-shape and commonly have lamellar twins and complex zoning patterns and many glass inclusions in large (more than 2 mm long) phenocrysts. Some large phenocrysts have extreme resorption; some phenocrysts have a ball-like shape. Groundmass minerals are mostly pl, and contain trace amounts of opx, cpx and mt. Groundmass glass is dark gray to black under open nicol. Pl in the groundmass has a columnar to acicular shape, low relief, and most of groundmass mineral has twin. It has almost parallel extinction and negative elongation. Cr-spinel is observed in some samples, only in glomerocrysts and

Table 2 Representative two-pyroxene and plagioclase analyses of Type A samples

Analytical no.	Core–rim	SiO_2	TiO_2	Al_2O_3	FeO	MnO	MgO	CaO	Na_2O	K_2O	Cr_2O_3	V_2O_3	NiO	P_2O_5	Total	Atomic ratio			
9R-1, 25–30 (Unit 3, bulk SiO_2 = 56.43 wt.%)																			
Opx phenocrysts																Wo%	En%	Fs%	Mg%
H1-36191	Rim	55.52	0.10	1.85	13.94	0.27	26.31	1.69	0.03	0.11	0.07	0.00	0.02	0.00	99.92	3.4	74.4	22.1	77.1
H1-36192	Core	54.22	0.06	0.89	13.86	0.32	28.05	1.69	0.03	0.03	0.03	0.03	0.10	0.03	99.32	3.3	75.7	21.0	78.3
H1-36193	Core	53.93	0.10	0.92	13.60	0.34	27.38	1.83	0.03	0.01	0.05	0.01	0.10	0.05	98.34	3.6	75.4	21.0	78.2
H1-36194	Core	54.07	0.07	0.98	13.76	0.34	27.52	1.83	0.03	0.02	0.10	0.03	0.04	0.04	98.82	3.6	75.3	21.1	78.1
H1-36195	Rim	54.35	0.11	1.04	13.96	0.30	27.87	1.72	0.03	0.01	0.06	0.00	0.06	0.07	99.58	3.4	75.4	21.2	78.1
H1-36296	Rim	54.56	0.10	1.18	14.16	0.31	27.56	1.75	0.02	0.00	0.01	0.02	0.06	0.00	99.74	3.4	75.0	21.6	77.6
H1-36297	Core	54.89	0.09	1.14	14.40	0.33	27.61	1.78	0.01	0.01	0.04	0.00	0.05	0.03	100.37	3.5	74.7	21.9	77.4
H1-36298	Core	55.01	0.06	0.97	14.41	0.29	27.68	1.60	0.03	0.01	0.01	0.03	0.11	0.00	100.19	3.1	75.0	21.9	77.4
H1-36299	Core	55.04	0.09	1.17	14.13	0.34	27.59	1.52	0.02	0.01	0.03	0.00	0.06	0.00	100.00	3.0	75.4	21.7	77.7
H1-36300	Rim	54.86	0.07	1.12	14.04	0.27	27.48	1.57	0.04	0.01	0.04	0.02	0.05	0.06	99.62	3.1	75.3	21.6	77.7
Cpx phenocrysts																Wo%	En%	Fs%	Mg%
H1-36066	Rim	53.41	0.08	1.67	6.68	0.21	17.22	19.76	0.24	0.01	0.13	0.00	0.09	0.11	99.61	40.4	49.0	10.7	82.1
H1-36067	Core	53.14	0.15	1.79	7.16	0.23	17.73	19.16	0.23	0.03	0.15	0.02	0.03	0.10	99.92	38.8	49.9	11.3	81.5
H1-36068	Core	53.33	0.15	1.70	6.73	0.20	17.07	19.43	0.22	0.00	0.12	0.02	0.06	0.08	99.10	40.1	49.0	10.9	81.9
H1-36069	Core	53.69	0.12	1.64	7.00	0.22	16.83	19.36	0.22	0.00	0.09	0.04	0.05	0.00	99.25	40.1	48.5	11.3	81.1
H1-36070	Rim	53.38	0.13	1.73	7.21	0.23	16.77	19.00	0.21	0.02	0.03	0.03	0.06	0.09	98.89	39.6	48.7	11.7	80.6
H1-36071	Rim	53.43	0.10	1.69	6.75	0.17	16.90	19.37	0.24	0.00	0.11	0.03	0.00	0.09	98.89	40.2	48.8	11.0	81.7
H1-36072	Core	53.33	0.16	1.91	7.30	0.18	17.11	19.04	0.23	0.01	0.02	0.04	0.06	0.13	99.51	39.2	49.0	11.7	80.7
H1-36073	Core	53.58	0.12	1.62	7.13	0.19	16.97	19.26	0.24	0.00	0.06	0.06	0.07	0.08	99.39	39.8	48.7	11.5	80.9
H1-36074	Core	52.59	0.20	3.13	7.65	0.16	15.73	19.83	0.26	0.01	0.02	0.04	0.03	0.10	99.75	41.6	45.9	12.5	78.6
H1-36075	Rim	53.24	0.16	2.16	7.08	0.13	16.50	19.99	0.20	0.00	0.14	0.04	0.03	0.08	99.73	41.2	47.4	11.4	80.6
Pl phenocrysts																An%	Ab%	Or%	
H1-36321	Rim	47.42	0.03	32.91	0.67	0.07	0.13	14.85	2.03	0.02	0.00	0.00	0.00	0.15	98.27	80.1	19.8	0.1	
H1-36322	Core	48.46	0.02	32.37	0.74	0.03	0.14	14.80	2.46	0.03	0.07	0.02	0.00	0.06	99.18	76.8	23.1	0.2	
H1-36323	Core	48.18	0.05	32.25	0.58	0.01	0.13	14.73	2.44	0.04	0.03	0.00	0.01	0.04	98.49	76.8	23.0	0.2	
H1-36324	Core	48.74	0.04	32.60	0.66	0.01	0.13	15.07	2.42	0.03	0.05	0.00	0.02	0.08	99.85	77.4	22.5	0.2	
H1-36325	Rim	48.17	0.01	32.93	0.63	0.06	0.12	15.56	2.20	0.13	0.00	0.02	0.00	0.08	99.90	79.0	20.2	0.8	
H1-36286	Rim	49.53	0.01	32.66	0.74	0.00	0.16	15.23	2.40	0.06	0.00	0.00	0.00	0.07	100.86	77.5	22.1	0.4	
H1-36287	Core	49.69	0.02	32.12	0.62	0.03	0.13	15.36	2.53	0.03	0.05	0.00	0.03	0.00	100.60	77.0	22.9	0.2	
H1-36288	Core	49.26	0.04	32.30	0.68	0.05	0.14	15.00	2.50	0.02	0.00	0.00	0.00	0.05	100.04	76.8	23.1	0.1	
H1-36289	Core	49.44	0.00	31.87	0.58	0.02	0.14	15.06	2.55	0.02	0.00	0.00	0.00	0.03	99.70	76.5	23.4	0.1	
H1-36290	Rim	47.70	0.00	32.40	0.60	0.04	0.14	15.28	2.10	0.05	0.00	0.00	0.00	0.05	98.36	79.9	19.8	0.3	
15R-2, 85–88 (Unit 5, bulk SiO_2 = 61.17 wt.%)																			
Opx phneocrysts																Wo%	En%	Fs%	Mg%
H1-51006	Rim	52.48	0.08	1.33	21.39	0.44	22.14	1.84	0.03	0.02	0.04	0.06	0.00	0.00	99.84	3.7	62.4	33.8	64.9
H1-51007	Core	52.91	0.07	0.70	21.83	0.52	21.42	1.77	0.03	–0.01	0.09	0.00	0.05	0.00	99.38	3.6	61.3	35.0	63.6
H1-51008	Core	52.14	0.14	1.26	22.30	0.56	21.11	1.69	0.02	0.01	0.03	0.04	0.12	0.00	99.41	3.5	60.6	35.9	62.8

Table 2 continued

Analytical no.	Core–rim	SiO_2	TiO_2	Al_2O_3	FeO	MnO	MgO	CaO	Na_2O	K_2O	Cr_2O_3	V_2O_3	NiO	P_2O_5	Total	Atomic ratio			
15R-2, 85–88 (Unit 5, bulk SiO_2 = 61.17 wt.%)																			
Opx phneocrysts																Wo%	En%	Fs%	Mg%
H1-51009	Core	52.49	0.13	1.05	21.52	0.54	21.43	1.72	0.04	0.01	0.02	0.04	0.00	0.00	98.99	3.6	61.7	34.8	64.0
H1-51010	Rim	52.41	0.08	0.96	20.65	0.40	22.52	1.77	0.05	0.01	0.07	0.06	0.00	0.00	98.98	3.6	63.7	32.7	66.0
H1-51321	Rim	52.39	0.09	2.16	23.20	0.51	19.26	2.12	0.37	0.02	0.03	0.06	0.02	0.00	100.23	4.5	57.0	38.5	59.7
H1-51322	Core	52.66	0.04	0.78	20.43	0.50	22.73	1.65	0.03	0.01	0.05	0.02	0.00	0.00	98.90	3.4	64.3	32.4	66.5
H1-51323	Core	51.83	0.08	1.05	21.40	0.51	22.69	1.75	0.01	0.00	0.04	0.03	0.04	0.00	99.45	3.5	63.1	33.4	65.4
H1-51324	Core	52.20	0.09	1.13	20.51	0.42	22.87	1.68	0.03	0.00	0.07	0.02	0.02	0.00	99.04	3.4	64.3	32.3	66.5
H1-51325	Rim	52.83	0.11	1.21	19.96	0.49	23.28	1.84	0.01	0.02	0.06	0.03	0.00	0.00	99.84	3.7	65.0	31.3	67.5
Cpx phenocrysts																Wo%	En%	Fs%	Mg%
H1-51136	Rim	51.67	0.12	1.72	10.99	0.29	14.20	19.77	0.29	0.03	0.07	0.05	0.00	0.00	99.17	41.1	41.1	17.8	69.7
H1-51137	Core	52.41	0.12	1.72	9.74	0.26	14.87	20.05	0.26	0.00	0.01	0.04	0.04	0.00	99.53	41.5	42.8	15.7	73.1
H1-51138	Core	52.19	0.12	1.84	10.59	0.19	14.50	19.77	0.31	0.04	0.17	0.05	0.00	0.00	99.78	41.0	41.8	17.1	70.9
H1-51139	Core	52.14	0.14	1.81	10.18	0.24	14.49	19.69	0.26	0.01	0.05	0.04	0.05	0.00	99.08	41.2	42.2	16.6	71.7
H1-51140	Rim	52.27	0.15	1.77	10.55	0.21	14.20	19.69	0.27	0.02	0.06	0.07	0.02	0.00	99.27	41.3	41.4	17.3	70.6
H1-51171	Rim	48.34	0.18	1.75	10.87	0.25	14.90	19.36	0.48	0.02	0.02	0.06	0.05	0.00	96.28	39.9	42.7	17.5	71.0
H1-51172	Core	50.75	0.16	1.81	10.46	0.29	14.63	19.91	0.28	0.02	0.04	0.05	0.06	0.00	98.45	41.1	42.0	16.9	71.4
H1-51173	Core	51.25	0.14	1.73	10.79	0.32	14.40	19.85	0.27	0.01	0.02	0.04	0.00	0.00	98.81	41.1	41.5	17.4	70.4
H1-51174	Core	52.35	0.12	1.52	8.91	0.22	16.01	20.17	0.22	0.02	0.10	0.04	0.02	0.00	99.71	40.8	45.1	14.1	76.2
H1-51175	Rim	51.39	0.15	1.69	10.65	0.27	14.57	19.93	0.28	-0.01	0.04	0.06	0.03	0.00	99.05	41.1	41.8	17.1	70.9
Pl phenocrysts																An%	Ab%	Or%	
H1-51241	Rim	53.00	0.00	29.46	0.70	0.04	0.12	12.90	4.16	0.04	0.06	0.00	0.00	0.00	100.47	63.0	36.8	0.3	
H1-51242	Core	48.93	0.00	31.76	0.77	0.03	0.10	15.48	2.47	0.02	0.07	0.02	0.02	0.00	99.68	77.5	22.4	0.1	
H1-51243	Core	48.75	0.00	31.85	0.76	0.03	0.08	15.72	2.43	0.04	0.01	0.00	0.05	0.00	99.73	78.0	21.8	0.3	
H1-51244	Core	49.48	0.00	30.87	0.76	0.00	0.10	15.03	2.85	0.04	0.07	0.00	0.00	0.00	99.19	74.3	25.5	0.2	
H1-51245	Rim	50.24	0.00	29.79	0.82	0.01	0.10	14.16	3.41	0.05	0.04	0.00	0.00	0.00	98.62	69.4	30.3	0.3	
H1-51216	Rim	51.10	0.00	29.77	0.80	0.05	0.11	14.22	3.19	0.04	0.06	0.00	0.00	0.00	99.35	70.9	28.8	0.3	
H1-51217	Core	48.21	0.00	31.94	0.80	0.03	0.08	16.20	2.07	0.03	0.06	0.00	0.05	0.00	99.47	81.1	18.7	0.2	
H1-51218	Core	48.23	0.00	31.93	0.78	0.00	0.09	16.39	2.06	0.03	0.02	0.00	0.12	0.00	99.65	81.3	18.5	0.2	
H1-51219	Core	49.18	0.00	31.77	0.83	0.01	0.09	15.68	2.49	0.04	0.02	0.00	0.03	0.00	100.13	77.5	22.3	0.2	
H1-51220	Rim	50.36	0.00	30.66	0.82	0.05	0.10	14.82	3.05	0.04	0.01	0.00	0.02	0.00	99.93	72.7	27.0	0.3	

One phenocryst analysis is divided by broken limes

Notes: opx and cpx: Wo% = Ca/(Ca + Mg + Fe); En% = Mg/(Ca + Mg + Fe); Fs% = Fe/(Ca + Mg + Fe); Mg# = Mg/(Mg + Fe), all in mol%. pl: An% = Ca/(Ca + Na + K); Ab% = Na/(Ca + Na + K); Or% = K/(Ca + Na + K), all in mol%

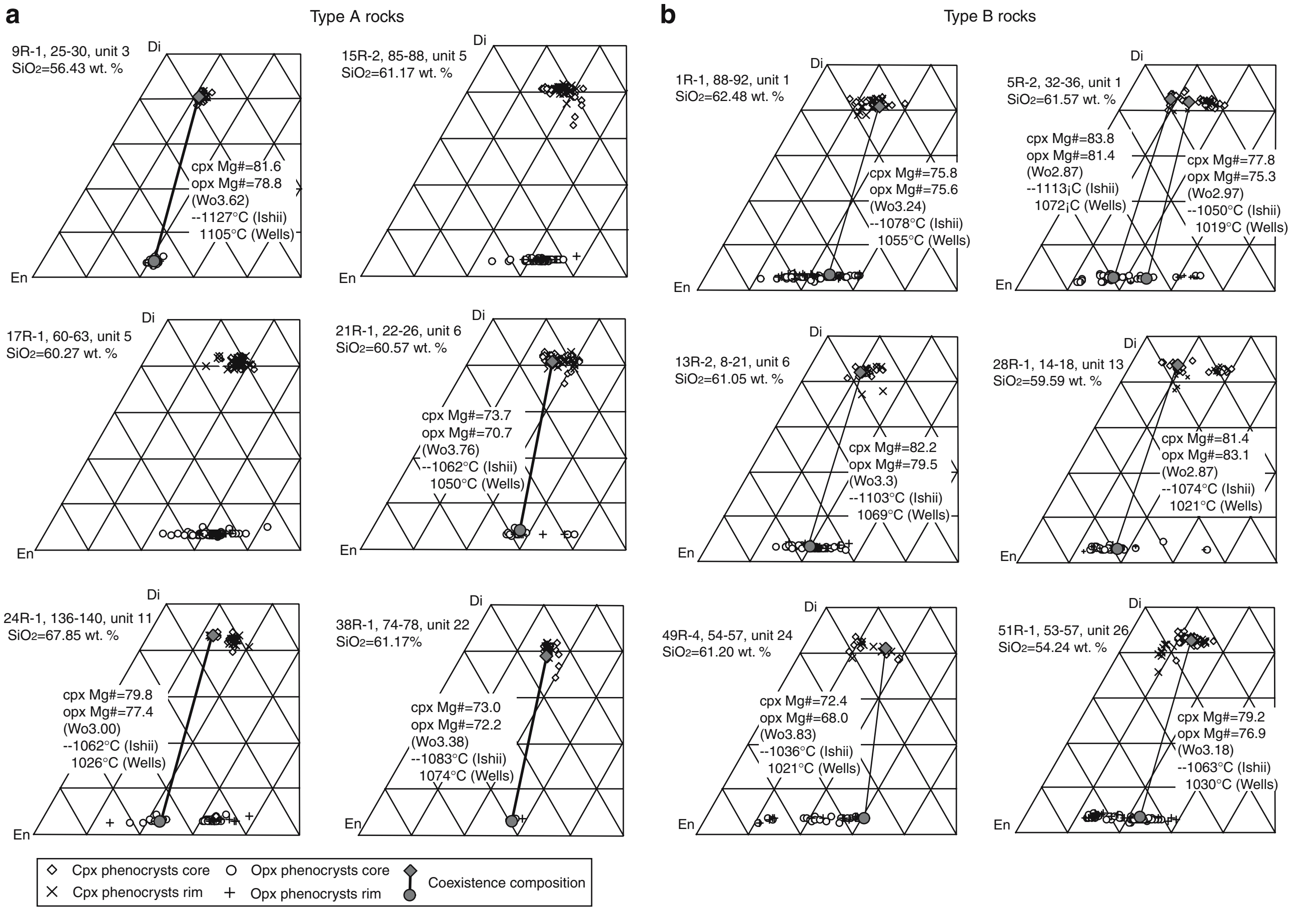

Fig. 4 Phonocryst compositions of pyroxene in the selected Type A (**a**) and Type B (**b**) rocks on pyroxene quadrilateral plots. Crystallization temperatures are estimated by two-pyroxene geothermometer by Ishii (1975, 1981) and Wells (1977)

inclusion in pyroxene phenocrysts. They are euhedral to anhedral and are isotropic with a red to dark red color in plane polarized light. However, mt is observed in all stages of the Type B rocks. They are euhedral to anhedral and commonly found as an opaque phase in the groundmass or as phenocrysts in evolved rocks.

Mineral chemistry

Type A samples

For the Type A rocks 18 samples were chosen for EPMA analysis (Table 1). Representative mineral analyses are shown in Table 2.

Figure 4a shows pyroxene compositions of the Type A phenocrysts on the pyroxene quadrilateral plots.

Typical opx phenocrysts in mafic samples show weak zoning, and core compositions are En (enstatite) 73–78 (Mg# = 75–81) and Wo (wollastonite) 3.0–3.5. Variation of phenocryst composition is narrow, and rim compositions are similar to core compositions. Those in felsic rocks are less magnesian than those in mafic rocks. Core compositions of typical phenocrysts in felsic rocks are Wo 3.5–4.0 and En 61–71 (Mg# = 63–73). Cpx phenocrysts in mafic samples show similar core and rim compositions. Core compositions of typical cpx phenocrysts are Wo 37–42 and En 51–48 (Mg# = 77–81). Those in felsic rocks are less magnesian than those in mafic rocks. Core compositions of typical phenocrysts in felsic rocks are Wo 39–41 and En 45–40 (Mg# = 63–68). Compositions of cpx phenocrysts slightly decrease in wollastonite component and increase ferrosilite component with decreasing Mg#. In felsic samples, crystallization of opx ceases at Mg# values of about 60, and that of cpx continues at Mg# about 50. Pl and pyroxene compositions are plotted in composition versus frequency diagrams, that is, pl is plotted in anorthite (An) content versus frequency diagrams and pyroxenes are plotted in Mg# versus frequency diagrams (Fig. 5a). Pl phenocrysts in mafic samples show the range An 70–85. Pl phenocrysts in the Type A rocks have less than 80% of An content,

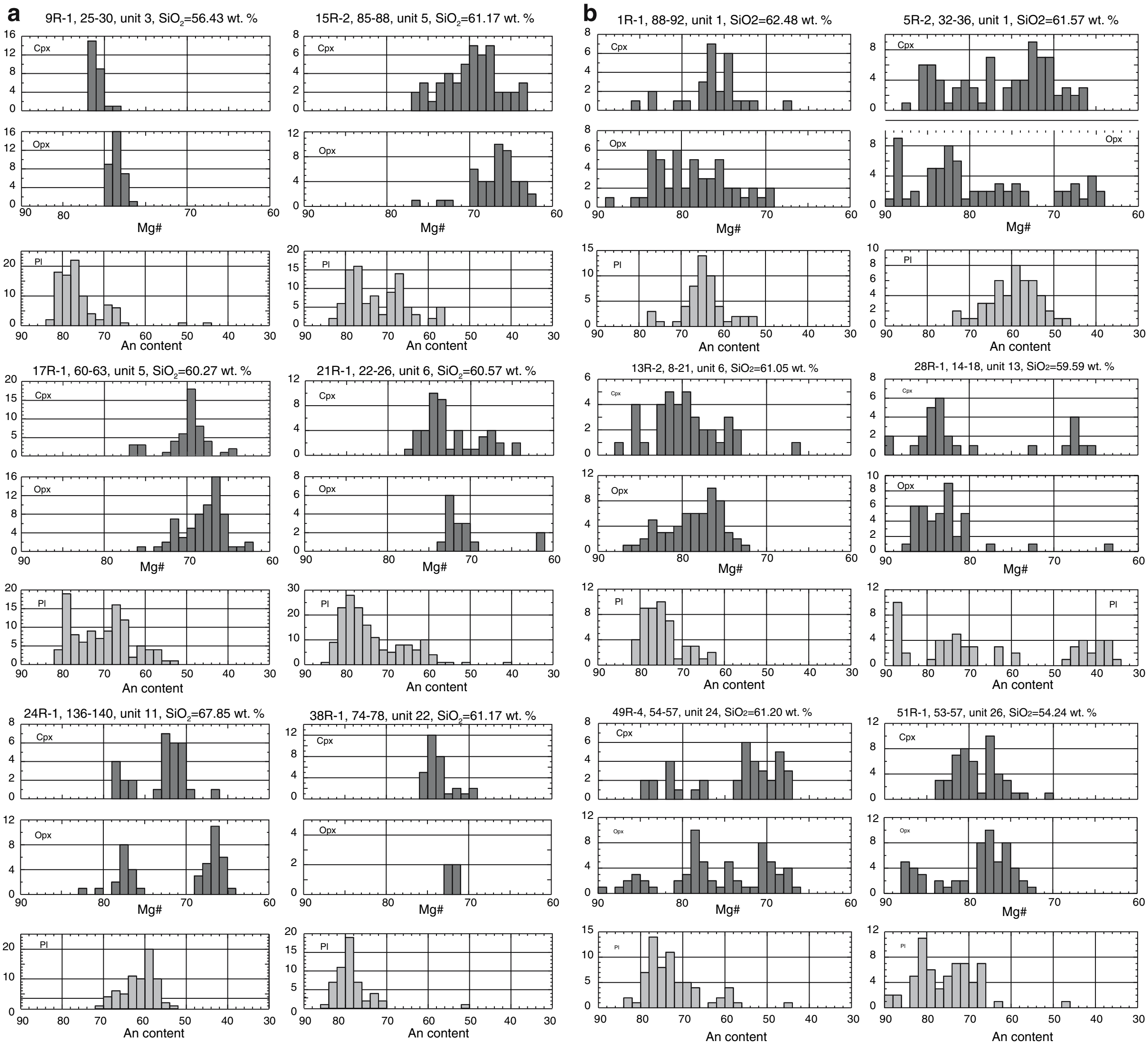

Fig. 5 Phenocryst compositions of pyroxene and plagioclase in the Type A (**a**) and Type B (**b**) rocks on compositional frequency diagrams. Pyroxene compositions are plotted into frequency against Mg# (cation Mg/(Mg + Fe) × 100), and pl compositions are plotted into frequency against anorthite (An) content

and those phenocrysts in felsic rocks have low An content than mafic rocks, core composition shows An 61–80.

Type B samples

For the Type B rocks 29 samples were chosen for EPMA analysis (Table 1). Representative mineral analyses are shown in Table 3.

Pyroxene compositions of the Type B are more complex than that of the Type A (Fig. 4b). In mafic samples of the Type B, core compositions of typical opx phenocrysts are En 70–89 (Mg# = 72–90) and Wo 2.0–3.5, and rim compositions are En 72–88 (Mg# = 74–88) and Wo 2.5–3.5. Core compositions of typical cpx phenocrysts are Wo 40–42 and En 42–48 (Mg# = 72–88) and rim compositions are Wo 41–43 and En 43–48 (Mg# = 88–75).

Generally, rim compositional ranges of both pyroxenes are narrower than the core range. In relatively felsic samples of Type B, mineral compositions are evolved, the most iron-rich opx and cpx composition are at Mg# = 65. Some samples have low-Ca cpx and high-Ca opx phenocrysts rim and groundmass minerals. It is assumed that these compositions of both pyroxenes reflect quenched trends.

Table 3 Representative two-pyroxene and plagioclase analyses of Type B samples

Analytical no.	Core–rim	SiO_2	TiO_2	Al_2O_3	FeO	MnO	MgO	CaO	Na_2O	K_2O	Cr_2O_3	V_2O_3	NiO	P_2O_5	Total	Atomic ratio			
51R-1, 53–57 (Unit 26, bulk SiO_2 = 54.24 wt.%)																			
Opx phenocrysts																Wo%	En%	Fs%	Mg#
H1-47001	Rim	55.99	0.05	0.99	9.47	0.24	30.91	1.86	0.01	0.00	0.28	0.00	0.11	0.00	99.92	3.6	82.3	14.1	85.3
H1-47002	Core	55.14	0.03	0.72	16.53	0.29	26.23	1.48	0.03	0.00	0.11	0.02	0.05	0.00	100.60	2.9	71.7	25.4	73.9
H1-47003	Core	54.49	0.06	1.10	16.03	0.34	26.20	1.47	0.01	0.00	0.09	0.02	0.05	0.00	99.87	2.9	72.3	24.8	74.4
H1-47004	Core	54.57	0.04	1.16	16.37	0.31	26.04	1.38	0.02	0.00	0.22	0.02	0.05	0.00	100.18	2.7	71.9	25.4	73.9
H1-47005	Rim	56.91	0.05	0.97	9.18	0.17	31.27	1.76	0.00	0.01	0.32	0.02	0.05	0.06	100.76	3.3	83.0	13.7	85.9
H1-47051	Rim	54.93	0.06	0.59	11.08	0.20	29.60	1.84	0.01	0.01	0.26	0.03	0.11	0.00	98.70	3.6	79.7	16.7	82.7
H1-47052	Core	54.25	0.08	1.07	16.33	0.34	26.37	1.33	0.02	0.00	0.13	0.02	0.04	0.00	99.97	2.6	72.3	25.1	74.2
H1-47053	Core	54.76	0.02	0.65	14.61	0.19	27.46	1.46	0.02	0.02	0.26	0.00	0.08	0.03	99.57	2.9	74.8	22.3	77.0
H1-47054	Core	54.13	0.09	1.08	15.54	0.26	26.44	1.27	0.03	0.00	0.29	0.02	0.04	0.03	99.21	2.5	73.3	24.2	75.2
H1-47055	Rim	55.37	0.08	1.93	11.69	0.21	28.98	2.02	0.04	0.00	0.00	0.03	0.00	0.00	100.35	3.9	78.3	17.7	81.5
Cpx phenocrysts																Wo%	En%	Fs%	Mg#
H1-47091	Rim	52.75	0.13	2.95	6.65	0.19	16.55	20.48	0.18	0.01	0.15	0.03	0.03	0.00	100.11	42.1	47.3	10.7	81.6
H1-47092	Core	52.27	0.16	2.12	8.73	0.19	14.79	20.48	0.22	–0.01	0.18	0.07	0.02	0.00	99.22	42.8	43.0	14.2	75.1
H1-47093	Core	52.21	0.18	2.45	9.15	0.17	14.65	20.69	0.28	0.02	0.25	0.05	0.00	0.00	100.10	42.9	42.3	14.8	74.1
H1-47094	Core	52.74	0.13	2.11	7.52	0.18	16.00	20.59	0.26	0.00	0.26	0.06	0.00	0.00	99.85	42.3	45.7	12.0	79.1
H1-47095	Rim	52.71	0.21	1.63	8.89	0.16	15.26	20.82	0.25	0.00	0.05	0.07	0.02	0.00	100.07	42.5	43.3	14.2	75.4
H1-47156	Rim	51.81	0.19	2.59	9.57	0.19	14.82	20.53–	0.23	0.00	0.00	0.11	0.07	0.00	100.10	42.2	42.4	15.4	73.4
H1-47157	Core	53.16	0.17	1.98	6.98	0.12	16.12	20.84	0.30	0.02	0.50	0.04	0.07	0.00	100.30	42.8	46.0	11.2	80.5
H1-47158	Core	53.05	0.15	1.96	8.63	0.21	15.43	21.22	0.22	0.00	0.07	0.04	0.00	0.00	100.99	42.9	43.4	13.6	76.1
H1-47159	Core	52.96	0.15	1.75	8.91	0.26	15.07	21.01	0.26	0.01	0.17	0.03	0.05	0.00	100.63	42.9	42.9	14.2	75.1
H1-47160	Rim	53.34	0.17	1.77	8.09	0.14	15.69	20.97	0.22	0.00	0.09	0.08	0.00	0.00	100.56	42.7	44.4	12.9	77.6
Pl phneocrysts																An%	Ab%	Or%	
H1-25116	Rim	49.52	0.00	31.22	0.73	0.00	0.12	15.09	3.29	0.05	0.00	0.00	0.03	0.00	100.03	71.6	28.2	0.3	
H1-25117	Core	47.52	0.00	32.34	0.59	0.00	0.08	16.61	2.34	0.01	0.04	0.00	0.00	0.00	99.53	79.6	20.3	0.1	
H1-25118	Core	49.60	0.00	31.29	0.78	0.00	0.08	15.58	3.09	0.05	0.02	0.00	0.00	0.00	100.49	73.4	26.3	0.3	
H1-25119	Core	49.58	0.00	31.22	0.77	0.00	0.08	15.31	3.00	0.04	0.10	0.00	0.00	0.00	100.09	73.7	26.1	0.2	
H1-25120	Rim	50.91	0.01	30.36	0.70	0.00	0.10	14.48	3.38	0.04	0.03	0.00	0.00	0.00	100.01	70.1	29.6	0.2	
H1-25121	Rim	48.78	0.00	30.97	0.68	0.00	0.11	15.54	2.67	0.05	0.00	0.00	0.00	0.00	98.78	76.1	23.6	0.3	
H1-25122	Core	45.82	0.00	33.73	0.52	0.00	0.04	18.19	1.29	0.02	0.02	0.00	0.00	0.00	99.63	88.5	11.4	0.1	
H1-25123	Core	48.34	0.04	32.11	0.65	0.00	0.07	16.64	2.16	0.04	0.00	0.00	0.00	0.00	100.05	80.8	19.0	0.2	
H1-25124	Core	47.88	0.00	32.91	0.60	0.00	0.08	17.76	1.94	0.02	0.05	0.00	0.00	0.00	101.23	83.4	16.5	0.1	
H1-25125	Rim	51.02	0.00	31.29	0.70	0.00	0.09	15.55	2.90	0.05	0.00	0.00	0.00	0.00	101.61	74.5	25.2	0.3	
1R-1, 88–92 (Unit 1, bulk SiO_2 = 62.48 wt.%)																			
Opx phenocrysts																Wo%	En%	Fs%	Mg#
H1-34271	Rim	68.50	0.05	0.81	13.13	0.34	28.07	1.84	0.03	0.01	0.21	0.00	0.06	0.00	99.45	3.6	76.4	20.0	79.2
H1-34272	Core	55.70	0.07	1.15	10.81	0.23	30.24	1.55	0.05	0.01	0.28	0.02	0.08	0.00	100.19	3.0	80.8	16.2	83.3
H1-34273	Core	55.43	0.09	1.23	10.83	0.31	30.41	1.53	0.01	0.02	0.20	0.00	0.07	0.06	100.18	2.9	80.9	16.2	83.4

Table 3 continued

Analytical no.	Core–rim	SiO_2	TiO_2	Al_2O_3	FeO	MnO	MgO	CaO	Na_2O	K_2O	Cr_2O_3	V_2O_3	NiO	P_2O_5	Total	Atomic ratio			
1R-1, 88–92 (Unit 1, bulk SiO_2 = 62.48 wt.%)																			
Opx phenocrysts																Wo%	En%	Fs%	Mg#
H1-34274	Core	55.87	0.06	1.11	10.33	0.25	30.29	1.53	0.02	0.01	0.22	0.00	0.07	0.00	99.76	3.0	81.5	15.6	83.9
H1-34275	Rim	55.67	0.04	1.17	11.84	0.28	30.02	1.29	0.03	0.01	0.38	0.00	0.08	0.00	100.81	2.5	79.9	17.7	81.9
H1-34406	Rim	53.43	0.12	1.08	15.71	0.35	25.78	1.47	0.03	0.01	0.15	0.00	0.04	0.04	98.20	3.0	72.3	24.7	74.5
H1-34407	Core	55.10	0.04	1.19	11.01	0.24	29.60	1.95	0.04	0.00	0.49	0.02	0.08	0.00	99.76	3.8	79.6	16.6	82.7
H1-34408	Core	55.05	0.08	1.08	10.99	0.24	29.51	1.39	0.03	0.02	0.30	0.02	0.05	0.00	98.77	2.7	80.5	16.8	82.7
H1-34409	Core	54.51	0.05	1.63	13.49	0.30	28.12	1.53	0.05	0.02	0.28	0.00	0.10	0.00	100.06	3.0	76.4	20.6	78.8
H1-34410	Rim	54.10	0.09	1.11	16.90	0.48	26.36	1.41	0.06	-0.01	0.17	0.02	0.03	0.00	100.71	2.8	71.5	25.7	73.5
Cpx phenocrysts																Wo%	En%	Fs%	Mg#
H1-34006	Rim	54.20	0.11	1.33	7.34	0.25	17.62	19.86	0.27	0.00	0.33	0.00	0.05	0.00	101.36	39.7	48.9	11.4	81.1
H1-34007	Core	53.21	0.20	1.55	8.69	0.26	15.65	21.19	0.26	0.01	0.06	0.06	0.02	0.00	101.15	42.6	43.8	13.6	76.3
H1-34008	Core	52.59	0.21	1.63	8.97	0.27	15.03	20.95	0.27	0.01	0.11	0.04	0.00	0.00	100.07	42.9	42.8	14.3	74.9
H1-34009	Core	52.63	0.17	2.02	8.05	0.19	15.80	20.87	0.29	0.00	0.35	0.04	0.07	0.00	100.47	42.5	44.7	12.8	77.8
H1-34010	Rim	53.54	0.11	1.48	6.72	0.23	17.00	21.17	0.25	0.02	0.21	0.03	0.03	0.00	100.76	42.3	47.3	10.5	81.9
H1-34026	Rim	52.80	0.14	1.85	7.81	0.24	15.94	20.75	0.34	0.02	0.33	0.00	0.03	0.04	100.28	42.3	45.2	12.4	78.4
H1-34027	Core	52.89	0.12	1.65	8.22	0.26	16.14	20.24	0.23	0.01	0.13	0.02	0.04	0.00	99.96	41.2	45.7	13.1	77.8
H1-34028	Core	52.46	0.19	1.26	11.96	0.33	13.76	20.08	0.33	0.02	0.12	0.03	0.02	0.00	100.56	41.4	39.4	19.2	67.2
H1-34029	Core	51.48	0.18	1.89	10.43	0.30	14.57	19.93	0.28	0.01	0.06	0.02	0.04	0.00	99.18	41.2	41.9	16.8	71.4
H1-34030	Rim	52.99	0.17	1.72	9.27	0.25	15.35	21.07	0.31	0.00	0.28	0.02	0.05	0.00	101.48	42.4	43.0	14.6	74.7
Pl phenocrysts																An%	Ab%	Or%	
H1-34186	Rim	49.02	0.00	32.06	0.66	0.03	0.10	15.99	2.55	0.03	0.03	0.00	0.02	0.00	100.47	77.5	22.3	0.2	
H1-34187	Core	52.19	0.02	30.20	0.70	0.04	0.08	13.80	3.63	0.05	0.03	0.00	0.04	0.00	100.78	67.5	32.2	0.3	
H1-34188	Core	53.95	0.01	29.09	0.55	0.02	0.12	12.79	4.10	0.32	0.01	0.00	0.02	0.00	100.99	62.1	36.1	1.9	
H1-34189	Core	52.71	0.00	30.02	0.72	0.00	0.14	13.65	3.76	0.03	0.01	0.00	0.05	0.00	101.07	66.7	33.2	0.2	
H1-34190	Rim	50.75	0.03	31.28	0.71	0.05	0.11	15.14	2.95	0.02	0.00	0.00	0.00	0.00	101.03	73.8	26.0	0.1	
H1-34326	Rim	51.97	0.01	29.95	0.74	0.00	0.13	12.63	3.84	0.04	0.04	0.00	0.00	0.09	99.42	64.4	35.6	0.3	
H1-34327	Core	51.86	0.04	29.95	0.65	0.01	0.08	12.71	3.72	0.05	0.00	0.00	0.00	0.05	99.12	65.2	34.5	0.3	
H1-34328	Core	52.84	0.00	29.43	0.55	0.01	0.10	12.21	4.06	0.05	0.00	0.00	0.00	0.08	99.33	62.3	37.4	0.3	
H1-34329	Core	53.58	0.03	28.74	0.70	0.02	0.11	11.86	4.48	0.08	0.05	0.00	0.00	0.05	99.69	59.2	40.4	0.5	
H1-34330	Rim	52.41	0.00	29.49	0.83	0.06	0.16	12.76	3.87	0.05	0.03	0.00	0.00	0.04	99.70	64.4	35.4	0.3	

One phenocryst analysis is divided by broken limes

Notes: opx and cpx: Wo% = Ca/(Ca + Mg + Fe); En% = Mg/(Ca + Mg + Fe); Fs% = Fe/(Ca + Mg + Fe); Mg# = Mg/(Mg + Fe), all in mol%. pl: An% = Ca/(Ca + Na + K); Ab% = Na/(Ca + Na + K); Or% = K/(Ca + Na + K), all in mol%

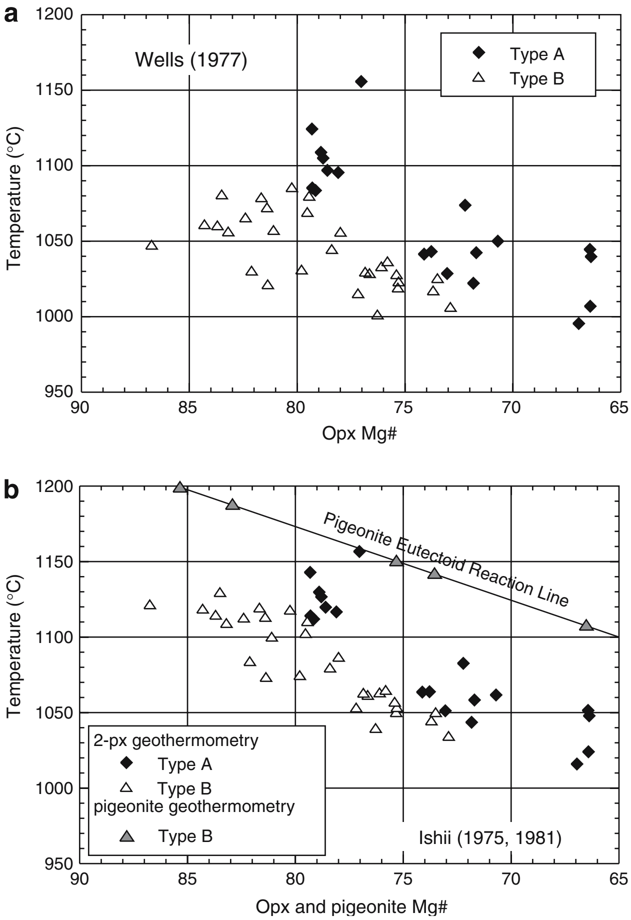

Fig. 6 Crystallization temperature of Type A and B rocks estimated by two-pyroxene geothermometer by Wells (1977) versus opx Mg# plots (**a**), and estimated by two-pyroxene and pigeonite geothermometer by Ishii (1975, 1981) versus opx and pigeonite Mg# plots (**b**)

Pl and pyroxene compositions are plotted in composition versus frequency diagrams, that is, pl is plotted in anorthite content versus frequency diagrams and pyroxenes are plotted in Mg# versus frequency diagrams (Fig. 5b). Opx, cpx and pl phenocrysts have wide range of compositions. High-An, more than 80% of An content, pl phenocrysts are present in many Type B samples, different from the Type A rocks. Unit 1 samples show low An content; core compositions of typical phenocrysts are An 40–70.

Two-pyroxene temperature in the Type A and B rocks

In the following, pyroxene compositions of the Type A rocks are compared with those of the Type B. Representative coexistence of two-pyroxene phenocryst core compositions in Type A and B, and estimated crystallization temperature by Wood and Banno (1973), Ishii (1975, 1981) and Wells (1977) are shown in Table 4.

Pyroxene compositions in Type B show wider two-phase region between Ca-rich and -poor pyroxene than Type A (Figs. 4, 5). Wo content of phenocrysts with Mg# = 79 in the Type A are 3.10–3.62, average is 3.46, those with Mg# = 73 are 3.27–3.39, average is 3.33 and those with Mg# = 66 are 3.36–3.55, average is 3.46. Crystallization temperatures are estimated for this type by two-pyroxene geothermometry on the basis of the chemistry of coexisting Ca-rich and Ca-poor pyroxenes, i.e., 1,125°C (Mg# = 79), 1,054°C (Mg# = 73) and 1,028°C (Mg# = 66) by geothermometer of Wells (1977), although Wo content of phenocrysts at Mg# = 80 are 2.97–3.64, average is 3.26, and those at Mg# = 75 are 2.70–3.17, average is 2.98. Crystallization temperatures for type B are estimated using two-pyroxene geothermometer, i.e., 1,098°C (Mg# = 80) and 1,052°C (Mg# = 75) by Wells (1977). Crystallization temperatures of both groups are different, those of Type A volcanic rocks are 50–100°C higher at the same Mg# than those of Type B in mafic composition, and similar temperature in felsic composition (Fig. 6a, b). The core of phenocrysts in each sample started to crystallize at equilibrium in the magma chamber. Its composition and crystallization temperature may also reflect fractional crystallization of the magma in the magma chamber. It may therefore be reasonable to assume that the temperatures estimated earlier correspond to the temperature in the magma chamber.

In the groundmass stage of Type B, pigeonite is observed in some samples. These pigeonite groundmass minerals show low Mg#, mainly lower than 75. Calculated crystallization temperature of pigeonite using the pigeonite geothermometer of Ishii (1975) yields 1,100–1,150°C (Fig. 6b). Some samples have very high Mg# (more than 80) pigeonite. Crystallization temperatures of pigeonite show 1,180–1,200°C (Fig. 6b). This pigeonite geothermometer can be used to estimate the crystallization of pyroxenes in the groundmass stage. It is notable that the estimated temperatures of the groundmass stage of crystallization are higher than those of the phenocryst stage. These observations show intrusion of high temperature magma into the magma chamber.

Bulk rock chemistry

Volcanic rocks at the Site 786 range from basalt (SiO_2 = 47 wt.%) to rhyolite (SiO_2 = 76 wt.%). Arculus et al. (1992) classified these rocks into eight groups based on the classification of boninites by

Fig. 7 Variation diagrams of bulk major elements for Type A and B rocks and the early arc volcanism in the Ogasawara and Mariana regions, the Chichi-Jima boninite and two-pyroxene andesite (Taylor et al. 1994), Haha-Jima basalt (Maehara and Maeda 2004), DSDP Leg 60 Site 458 boninite and tholeiite (Wood et al. 1982) and Guam boninite (Reagan and Meijer 1984). These data are normalized as water-free condition and Fe oxide as total Fe_2O_3. TiO_2 content of Site 458 tholeiite is more than 1.0% (1.05–1.18%)

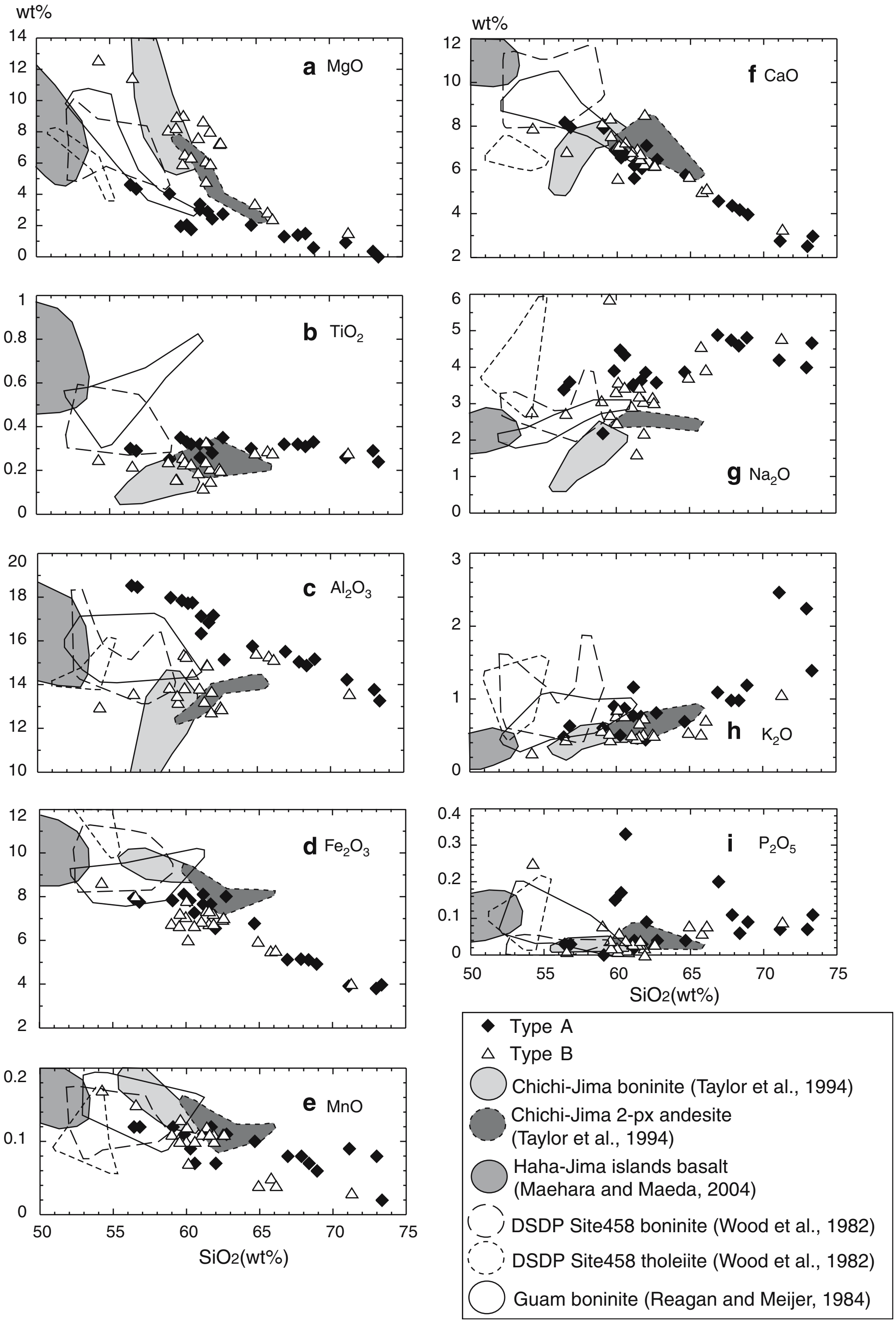

Crawford et al. (1989) and other rocks conforming to Reagan and Meijer (1984), Hickey-Vargas (1989) and Umino (1985, 1986), including low-Ca boninite (LCB), intermediate-Ca boninite (ICB), high-Ca boninite (HCB), low-Ca bronzite andesite (LCBrzA), intermediate-Ca bronzite andesite (ICBrzA), andesite (A), dacite (D) and rhyolite (R). Murton et al. (1992) divided these groups into four series, LCB (Low-Ca boninite) series, ICB series (Intermediate-Ca boninite), ADR (andesite, dacite and rhyolite) series, and Late dike series.

Compared to bulk compositions of Types A and B, we selected major and trace element analysis data near the location of EPMA analyzed samples (Table 1) from Arculus et al. (1992) and Murton et al. (1992). These data are shown in Tables 5, 6.

Table 4 Representative analyzes of coexistence opx and cpx compositions, and estimated temperature by Wood and Banno (1973), Ishii (1975, 1981) and Wells (1977)

Type	Type A										Type B	
Sample ID	9R-1, 25–30		21R-1, 22–26		24R-1, 136–140				38R-1, 74–78		1R-1, 88–92	
Anal. no.	H1-36132	H1-36131	H1-43360	H1-43355	H1-45117	H1-45118	H1-45119	H1-45120	H1-24035	H1-24030	H1-34151	H1-34152
Mineral	cpx	opx	cpx	opx	cpx	opx	cpx	opx	cpx	opx	cpx	opx
wt.%												
SiO_2	53.63	55.16	53.11	53.90	52.77	54.66	53.06	54.81	51.87	53.77	53.03	54.52
TiO_2	0.10	0.07	0.14	0.10	0.14	0.07	0.16	0.05	0.12	0.10	0.15	0.08
Al_2O_3	1.60	1.43	1.96	1.32	1.98	1.16	1.82	1.19	1.92	1.11	1.26	1.02
FeO	6.77	13.43	10.06	18.05	7.25	14.41	7.82	14.03	10.32	17.27	8.92	15.34
MnO	0.21	0.22	0.27	0.38	0.13	0.33	0.23	0.32	0.23	0.26	0.22	0.49
MgO	16.89	28.08	15.50	24.37	16.03	27.69	15.61	27.72	15.67	25.18	15.67	26.64
CaO	19.49	1.86	20.07	1.88	21.18	1.53	21.57	1.53	19.34	1.70	19.92	1.64
Na_2O	0.19	0.04	0.26	0.00	0.20	0.00	0.32	0.03	0.25	0.03	0.20	0.02
K_2O	0.00	0.00	0.02	0.00	0.02	0.01	0.02	0.04	0.03	0.02	0.03	0.01
Cr_2O_3	0.09	0.00	0.00	0.04	0.00	0.06	0.00	0.04	0.04	0.03	0.00	0.00
V_2O_3	0.13	0.09	0.04	0.00	0.37	0.15	0.11	0.12	0.01	0.00	0.05	0.08
NiO	0.09	0.05	0.00	0.00	0.00	0.03	0.00	0.02	0.04	0.06	0.10	0.03
P_2O_5	0.03	0.02	0.02	0.00	0.02	0.00	0.00	0.00	0.00	0.00	0.02	0.00
Total	99.22	100.43	101.44	100.04	100.09	100.10	100.73	99.89	99.86	99.52	99.57	99.87
Atomic %												
Mg#	81.60	78.80	73.30	70.70	79.80	77.40	78.10	77.90	73.03	72.22	75.80	75.60
Wo content	40.37	3.62	40.54	3.76	43.10	2.98	43.66	3.00	39.31	3.38	40.92	3.24
En content	48.67	75.99	43.58	68.00	45.38	75.10	43.98	75.55	44.32	69.78	44.79	73.14
Fs content	10.95	20.39	15.87	28.24	11.52	21.93	12.36	21.45	16.37	26.84	14.30	23.62
Temperature												
Wood and Banno (1973)	1,087		1,004		1,022		1,003		1,028		1,032	
shii (1975, 1981)	1,127		1,062		1,062		1,040		1,083		1,078	
Wells (1977)	1,105		1,050		1,026		995		1,074		1,055	

Type	Type B											
Sample ID	5R-2, 32–36				13R-2, 8–21		28R-1, 14–18		49R-4, 54–57		51R-1, 53–57	
Anal. no.	H1-9035	H1-9036	H1-9048	H1-9047	H1-11042	H1-11043	h1-15166	h1-15165	H1-26294	H1-26293	H1-47288	H1-47287
Mineral	cpx	opx	cpx	opx	cpx	opx	cpx	opx	cpx	opx	cpx	opx
wt. %												
SiO_2	52.45	54.59	52.77	55.11	53.14	54.63	54.19	55.99	51.50	53.14	53.13	54.76
TiO_2	0.07	0.04	0.12	0.09	0.08	0.04	0.11	0.04	0.18	0.10	0.17	0.11
Al_2O_3	1.59	0.81	1.88	1.11	1.20	0.92	1.69	1.22	1.79	0.86	1.96	1.10
FeO	7.99	15.72	5.81	12.21	6.38	12.97	5.85	11.62	10.29	19.82	7.47	14.33
MnO	0.24	0.41	0.18	0.26	0.23	0.37	0.18	0.25	0.19	0.29	0.18	0.24
MgO	15.71	26.92	16.89	29.97	16.54	28.26	16.16	28.47	15.12	23.58	15.92	26.70
CaO	20.76	1.52	20.48	1.52	19.97	1.68	21.09	1.44	20.37	1.92	20.90	1.59
Na_2O	0.26	0.05	0.23	0.05	0.19	0.04	0.24	0.03	0.27	0.06	0.25	0.02
K_2O	0.00	0.01	0.03	0.01	0.01	0.00	0.01	0.01	0.01	0.00	0.00	0.00

Table 4 continued

Type	Type B											
Sample ID	5R-2, 32–36				13R-2, 8–21		28R-1, 14–18		49R-4, 54–57		51R-1, 53–57	
Anal. no.	H1-9035	H1-9036	H1-9048	H1-9047	H1-11042	H1-11043	h1-15166	h1-15165	H1-26294	H1-26293	H1-47288	H1-47287
Mineral	cpx	opx	cpx	opx	cpx	opx	cpx	opx	cpx	opx	cpx	opx
Cr_2O_3	0.26	0.16	0.33	0.38	0.29	0.23	0.19	0.13	0.12	0.00	0.19	0.09
V_2O_3	0.00	0.02	0.00	0.00	0.00	0.00	0.04	0.00	0.04	0.03	0.05	0.03
NiO	0.06	0.04	0.08	0.05	0.11	0.16	0.00	0.00	0.02	0.02	0.06	0.06
P_2O_5	0.00	0.00	0.00	0.00	0.00	0.00	0.00	0.03	0.00	0.05	0.00	0.00
Total	99.39	100.28	98.79	100.75	98.11	99.29	99.74	99.22	99.90	99.86	100.28	99.01
Atomic %												
Mg#	77.80	75.33	83.82	81.40	82.22	79.53	83.13	81.37	72.37	67.97	79.16	76.85
Wo content	42.49	2.97	42.20	2.87	41.63	3.29	43.82	2.87	41.20	3.83	42.76	3.18
En content	44.74	73.10	48.44	79.06	47.99	76.91	46.71	79.03	42.55	65.37	45.31	74.41
Fs content	12.77	23.93	9.35	18.07	10.38	19.79	9.48	18.10	16.25	30.81	11.93	22.41
Temperature												
Wood and Banno (1973)	1,006		1,081		1,066		1,043		973		1,022	
Ishii (1975, 1981)	1,050		1,113		1,103		1,074		1,036		1,063	
Wells (1977)	1,019		1,072		1,069		1,021		1,021		1,030	

Type A is approximately equivalent to ADR series, and Type B is approximately equivalent to ICB series. But some ADR series rocks are classified into Type B (Table 5).

Type A and B volcanic rocks have different MgO concentrations in the Harker-type diagram (Fig. 7a). Type B samples have 12.6–1.5 wt.% of MgO versus 54.2–71.2 wt.% of SiO_2, and Type A samples have 4.7–0.1 wt.% of MgO versus 56.3–76.2 wt.% of SiO_2. Types A and B have different trends in this diagram; Type B rocks have high MgO in mafic compositions, rapidly decreasing with growing SiO_2 content, indicating rapid fractionation of mafic minerals. On the other hand, Type A rocks have low MgO in mafic rocks. Both series show similar characteristics in the compatible trace elements, especially Cr (Fig. 7a, b).

Both types show different trends in the Al_2O_3–SiO_2 diagram (Fig. 7c). Type B has low content of Al_2O_3 (12.8–15.4 wt.%), increasing with growing SiO_2 content at 63% of SiO_2. This characteristic indicates plagioclase-free fractionation. Type A shows high content (13.3–18.5 wt.%) and different gradually decreasing trend in this diagram. Sr content shows similar characteristics to Al_2O_3 (Fig. 8e). These distinct fractional trends of MgO and Al_2O_3 in Type B are one of the characteristics of boninite; Type B rocks are assumed boninite series.

TiO_2 contents of both series are low (Fig. 7b); these low concentrations of TiO_2 are one of the special features of boninite (e.g., Crawford et al. 1989). However, Type A samples have slightly higher TiO_2 content (0.25–0.35 wt.%) than Type B samples (0.13–0.33 wt.%).

Both series show depleted and slightly different high-field-strength element (HFSE) composition (Fig. 8f, g). The Type A rocks show slightly higher contents of Y (9–16 ppm) than Type B rocks (5–14 ppm), and the Zr contents of the Type A rocks are higher (48–84 ppm) than that of the Type B rocks (31–70 ppm). However, the difference in Zr/Y ratios between Types A and B is unclear in the basic stage (Fig. 9d). It is considered that Types A and B at the Site 786 have similar depleted parent materials because Y and Zr have similar behavior in partial melting processes.

Some samples show high P_2O_5 and Y contents (Figs. 7i, 8f). This anomalous enrichment was pointed by Murton et al. (1992). They found that these samples were found only within the breccia horizons, and similar style of enrichment was documented from lavas at Leg 126 Site 793 (Taylor et al. 1992). Teylor et al. attributed that the anomalous behavior of P and Y is associated with the breakdown of glass to smectite

Table 5 Comparison of Type A and B classification with schematic lithographic section by Arculus et al. (1992)

Arculus et al. (1992)				This study
Subunit no.	Section	Depth (mbsf)	Lithology	Type
1	1R-1, 0 cm–5R-2, 67 cm	162.5–200.8	ICBrzA breccia	Type B
2	5R-2, 67 cm–7R-1, 0 cm	200.8–217.8	HCB intrusion	
3	7R-1, 0 cm–10R-1, 0 cm	217.8–246.6	A breccia	Type A
4	10R-1, 0 cm–14R-1, 8 cm	246.6–285.5	ICB/BrzA breccia	Type B
5	14R-1, 8 cm–17R-1, 100 cm	285.5–315.3	A/D breccia	Type A
6	17R-1, 100 cm–21-1, 50 cm	315.3–353.5	A flow	Type A
7	20R-1, 42–90 cm	343.7–344.2	ICB intrusion	
8	21R-1, 50 cm–21R-2, 40 cm	353.5–355.4	R flow	Type A
9	21R-2, 40 cm–22R-1, 27 cm	353.4–362.9	HCB intrusion	
10	22R-1, 27 cm–23R-1, 0 cm	362.9–372.3	Sandstone	
11	23R-1, 0 cm–27R-1, 100 cm	372.3–411.8	D flow	Type A
12	27R-1, 100 cm–27R-2, 0 cm	411.8–412.3	Sandstone	
13	27R-2, 0 cm–32R-2, 55 cm	412.3–461.1	ICBrzA flow	Type B
14	29R-1, 40–70 cm	430.5–430.8	HCB intrusion	
15	30R-2, 75 cm–30R-3, 21 cm	442.0–442.9	HCB intrusion	
16	32R-2, 55 cm–34R-2, 15 cm	461.1–480.0	R flow	Type A
17	33R-1, 0–38 cm	468.7–469.1	HCB intrusion	
18	34R-1, 64–85 cm	478.9–479.2	Sandstone	
19	34R-2, 15 cm–34R-4, 100 cm	480.0–483.8	HCB intrusion	
20	34R-4, 100 cm–37R-1, 0 cm	483.8–507.4	D-R flow	Type B
21	37R-1, 0 cm–37R-3, 31 cm	507.4–510.7	ICB intrusion	
22	37R-3, 31 cm–40R-1, 65 cm	510.7–537.0	A flow/breccia	Type A
23	40R-1. 65 cm–40R-4, 30 cm	537.0–541.1	HCB intrusion	
24	40R-4, 30 cm–51R-1, 0 cm	541.1–642.2	ICBrzA flow/breccia	Type B
25	44R-1, 0 cm–44R-2, 10 cm	574.6–576.2	ICB intrusion	
26	51R-1, 0 cm–55R-2, 60 cm	642.2–682.9	ICB/BrzA breccia	Type B
27	55R-2, 60 cm–63R-2, 0 cm	682.9–749.5	LCB/BrzA pillow	
28	61R-4, 42 cm–61R-6, 40 cm	733.6–736.6	R intrusion	
29	63R-2, 0 cm–68R-1, 0 cm	749.5–796.3	R intrusion	
30	64R-2, 128 cm–65R-1, 75 cm	760.5–768.2	A intrusion	
31	67R-1, 8 cm–10 cm	786.8–786.8	ICB intrusion	
32	67R-1, 50 cm–80 cm	787.2–787.5	ICB intrusion	
33	68R-1, 0 cm–72R-2, 150 cm	796.3–826.6	LCBrzA intrusion	
34	72R-1, 0 cm–12 cm	823.6–823.7	ICBrzA intrusion	

during post-eruption fluid-rock interaction. We considered that phenocryst compositions are not affected under this process.

Types A and B have different trends in other type plots. In the AFM diagram (Kuno 1953; Fig. 10a) and Miyashiro (1974; Fig. 10b) plot, Type A has total FeO-enriched trend in the AFM diagram and increasing FeO/MgO trend in the Miyashiro diagram. These are one of the characteristics of tholeiite. We considered that Type A rocks are tholeiite series because of their bulk chemical characteristics, mineral assemblages (hydrous mineral-free in all samples) and mineral features indicating high crystallization temperatures of pyroxene.

Comparison to other IBM arc volcanics

The two series at Site 786 are compared with boninite and two-pyroxene andesite in the Chichi-Jima Island (Taylor et al. 1994), basalt in the Haha-Jima Islands (Maehara and Maeda 2004) and the Ogasawara Islands, boninite and tholeiite at the DSDP Leg 60 Site 458 in the central Mariana forearc region (Wood et al. 1982) and boninite in the Guam Island (Reagan and Meijer 1984) (Figs. 7–9).

Compared to the boninites in the IBM arc, the Chichi-Jima boninite shows the most typically boninitic geochemical characteristics. Boninite in the Izu foreaec (Type B) shows similar trend to the typically boninite in the Chichi-Jima. But MgO enrichment and Al_2O_3 depletion are not remarkable compared to the Chichi-Jima boninite. On the other hand, Type A shows similar MgO trend to boninite in the Mariana region, and different high Al_2O_3 content trend to other series.

Boninite and tholeiite series were active at the same time in the central Mariana forearc region (DSDP Site 458). Compared to the Site 786, both series show different incompatible element composition at the Site 458, different from the characteristics of Site 786 volcanism.

Table 6 Selected major and trace element analysis data near the location of EPMA analyzed samples (Table 1) from Arculus et al. (1992) and Murton et al. (1992)

Core	Interval (cm)	Depth (mbsf)	Lith. unit	Rock name	Type	SiO_2	TiO_2	Al_2O_3	Fe_2O_3	MnO	MgO	CaO	Na_2O	K_2O	P_2O_5	Total	Ni	Cr	V	Zn	Cu	Sc	Ga	Rb	Sr	Y	Zr	Ba	Nb
1R-1	61–64	163.1	1	ICBrzA Flow	B	61.86	0.21	12.75	7.23	0.11	8.03	6.27	3.06	0.52	0.02	100.06	99	374	177	55	67			6.3	174	6.2	44	36	2
1R-1	89–93	163.4	1	ICBrzA Flow	B	62.48	0.21	12.99	6.97	0.11	7.26	6.21	3.17	0.52	0.03	99.95	96	471	153	58	62	24	9	8	167	7	40	54	1
2R-1	72–76	170.2	1	ICBrzA Flow	B	62.57	0.20	12.90	7.04	0.11	7.29	6.22	3.03	0.50	0.03	99.89	100	471	146	58	63	25	8	8.6	191	7	41	43.6	0.6
3R-1	94–97	180.1	1	ICBrzA Flow	B	60.04	0.23	13.86	7.82	0.12	9.05	5.62	2.48	0.85	0.01	100.08	85	405	163	60	74	25	11	7	170	6	44	67	2
5R-1	23–25	198.8	1	ICBrzA Flow	B	59.99	0.26	15.38	7.09	0.10	5.95	7.09	3.33	0.77	0.02	99.98	61		151		68	21		13	173	6.1	44	22.4	0.7
5R-2	1–6	200.1	1	ICBrzA Flow	B	61.57	0.24	14.92	6.76	0.11	6.13	6.52	3.21	0.49	0.03	99.98	64	238	157	64	55	22	12	7	198	9	49	58	1
8R-1	43–44	228	3	A Berccia	A	56.82	0.29	18.46	7.76	0.12	4.34	7.95	3.59	0.63	0.03	99.99													
9R-1	10–15	237.2	3	A Berccia	A	59.09	0.25	17.98	7.83	0.12	4.03	7.92	2.18	0.60	0.00	100.00	40	8	239	72	101			7	226	10	53	40	2
9R-1	15–17	237.3	3	A Berccia	A	56.43	0.30	18.53	7.93	0.12	4.61	8.17	3.38	0.48	0.03	99.98	55		207		90	25		7.9	234	9.6	49	21.1	0.7
11R-1	122–126	257.5	4	ICB/BrzA Breccia	B	56.56	0.22	13.59	8.04	0.15	11.47	6.85	2.73	0.44	0.01	100.06	147	471	174	71	30	25		7.2	159	5.1	40	20.8	0.80
12R-2	120–124	268.6	4	ICB/BrzA Breccia	B	61.39	0.12	13.24	7.37	0.12	8.68	6.96	1.62	0.46	0.03	99.99	116	425	187	53	74			6	166	7	37	37	2
13R-2	134–138	278.5	4	ICB/BrzA Breccia	B	61.05	0.19	13.84	6.87	0.11	7.63	6.84	2.93	0.51	0.03	100.00	123	473	139	57	61	24	9	7.6	200	5.6	38	40.1	0.60
15R-2	3–8	296.5	5	A Breccia	A	61.17	0.32	17.13	7.66	0.11	3.02	6.21	3.52	0.77	0.04	99.95	20	8	214	78	77	22	16	13	257	9.7	58	44.9	1
16R-1	135–138	306	5	A Breccia	A	64.68	0.30	15.76	6.78	0.10	2.03	5.77	3.86	0.69	0.04	100.01													
16R-2	12–17	306.2	5	A Breccia	A	61.69	0.32	16.84	7.66	0.12	2.88	6.07	3.63	0.76	0.03	100.00	17	15	205	80	80	27	14	9	217	9	57	39	1
17R-1	67–69	315	5	A Breccia	A	60.27	0.33	17.72	7.83	0.09	2.03	6.56	4.47	0.50	0.17	99.97	13	10	219	76	69	23	17	6	248	35	61	77	1
21R-1	26–29	353.3	6	A Flow	A	59.86	0.35	17.85	8.11	0.11	1.95	6.91	3.90	0.90	0.15	100.09	18	5	210	86	62			11	244	19	59	35.4	1.4
21R-1	26–30	353.3	6	A Flow	A	60.57	0.32	17.75	7.27	0.07	1.75	6.71	4.33	0.87	0.33	99.97	16	17	190	59	78	21	16	13	233	28	56	54	
21R-1	129–131	354.3	8	R Flow	A	72.99	0.29	13.77	3.81	0.08	0.34	2.51	3.99	2.24	0.07	100.09	7		24	49	52	8		29	134	11	84	56.5	1.3
21R-2	28–32	354.7	8	R Flow	A	71.12	0.26	14.23	3.92	0.09	0.92	2.76	4.19	2.46	0.07	100.02	12	3	63	54	94	11	10	39	154	12	82	81.6	1.1
24R-1	41–45	383.2	11	D Flow	A	67.85	0.32	15.04	5.15	0.08	1.39	4.36	4.74	0.98	0.11	100.02	7	14	153	49	49	19	15	13	199	15	71	80	1
25R-1	64–72	392.1	11	D Flow	A	66.93	0.32	15.51	5.13	0.08	1.29	4.58	4.88	1.09	0.20	100.01	7	7	342	48	37	16	14	38	207	12	72	77.2	1.1
26R-1	68–70	401.9	11	D Flow	A	68.93	0.33	15.17	4.93	0.06	0.57	3.96	4.81	1.19	0.09	100.04	2		119	40	22			16	195	12	75	73	2
27R-1	31–35	411.1	11	D Breccia	A	68.37	0.31	14.87	5.11	0.07	1.48	4.17	4.59	0.98	0.06	100.01													
28R-1	15–18	420.6	13	ICBrzA Flow	B	59.59	0.16	13.19	7.23	0.13	8.97	7.57	2.70	0.44	0.02	100.00	134	491	153	58	62	31	8	6	192	5	33	36	1
30R-1	7–9	439.8	13	ICBrzA Flow	B	59.00	0.24	13.87	6.78	0.11	8.11	8.15	3.08	0.57	0.08	99.99	136	524	166	65	29	31	11	9	207	5	33	56	
30R-1	119–121	440.9	13	ICBrzA Flow	B	61.89	0.15	13.69	6.76	0.10	5.95	8.54	2.19	0.74	0.00	100.01	127	443	142	51	13			16	178	8	42	45	2
31R-1	84–86	450.2	13	ICBrzA Flow	B	59.54	0.16	13.50	6.67	0.10	8.27	8.37	5.87	0.53	0.04	103.05	131	382	184	63	20			10	211	6	34	32	2
32R-2	86–88	461.4	16	R Flow	A	73.36	0.24	13.27	3.98	0.02	0.00	2.97	4.66	1.39	0.11	100.00	2		46	39	20			43	173	12	74	77	1
35R-1	73–76	488.7	20	D–R Flow	B	64.92	0.28	15.44	5.96	0.04	3.38	5.70	3.72	0.54	0.08	100.06	26	50	152	48	34			8	213	10	56	59	2
35R-2	1–7	489.5	20	D–R Flow	B	65.78	0.29	15.31	5.53	0.05	2.86	5.01	4.57	0.52	0.06	99.98	19	43	121	64	58	16	12	8	201	10	62	80	1
35R-2	122–126	490.7	20	D–R Flow	B	66.12	0.28	15.16	5.55	0.04	2.43	5.15	3.93	0.71	0.08	99.45	24	47	134	48	55			12	187	9	60	42.7	1.3
36R-1	52–59	498.2	20	D–R Flow	B	71.29	0.28	13.59	4.03	0.03	1.54	3.29	4.79	1.06	0.09	99.99	5	14	56	51	21	12	12	22	171	13	70	80	1
38R-1	57–60	517.9	22	A Flow	A	61.17	0.26	16.34	8.11	0.11	3.36	5.63	3.48	1.16	0.02	99.64													
39R-1	47–53	527.3	22	A Flow	A	62.00	0.28	17.16	6.55	0.07	2.44	7.11	3.85	0.44	0.09	99.99	14	11	238	112	32	24	14	5	236	11	47	53	
39R-2	119–123	529.5	22	A Flow	A	62.73	0.35	15.14	8.01	0.11	2.73	6.47	3.58	0.81	0.04	99.97	15	11	270	67	108	26	13	16	173	11	48	54	1
42R-2	15–21	558.3	24	ICBrzA Flow	B	60.13	0.24	15.29	6.03	0.07	6.57	7.13	3.59	0.86	0.06	99.97	88	387	171	52	39	27	14	9	191	8	42	66	
43R-2	100–115	567.3	24	ICBrzA Flow	B	60.57	0.23	14.47	6.68	0.10	6.37	7.28	3.45	0.77	0.04	99.96	68	282	117	36	10	18	9	7	140	6	31	46	
45R-1	41–49	584.9	24	ICBrzA Breccia	B	61.59	0.33	14.90	7.36	0.11	4.82	6.74	3.45	0.67	0.04	100.01	66	193	258	62	99	25	13	18	193	9.8	45	557	0.80
51R-1	51–55	642.7	26	ICB Breccia	B	54.24	0.25	12.98	8.65	0.17	12.59	7.92	2.78	0.26	0.25	100.09	182	659	228	70	30	26		3.6	164	17	37	19.2	0.8

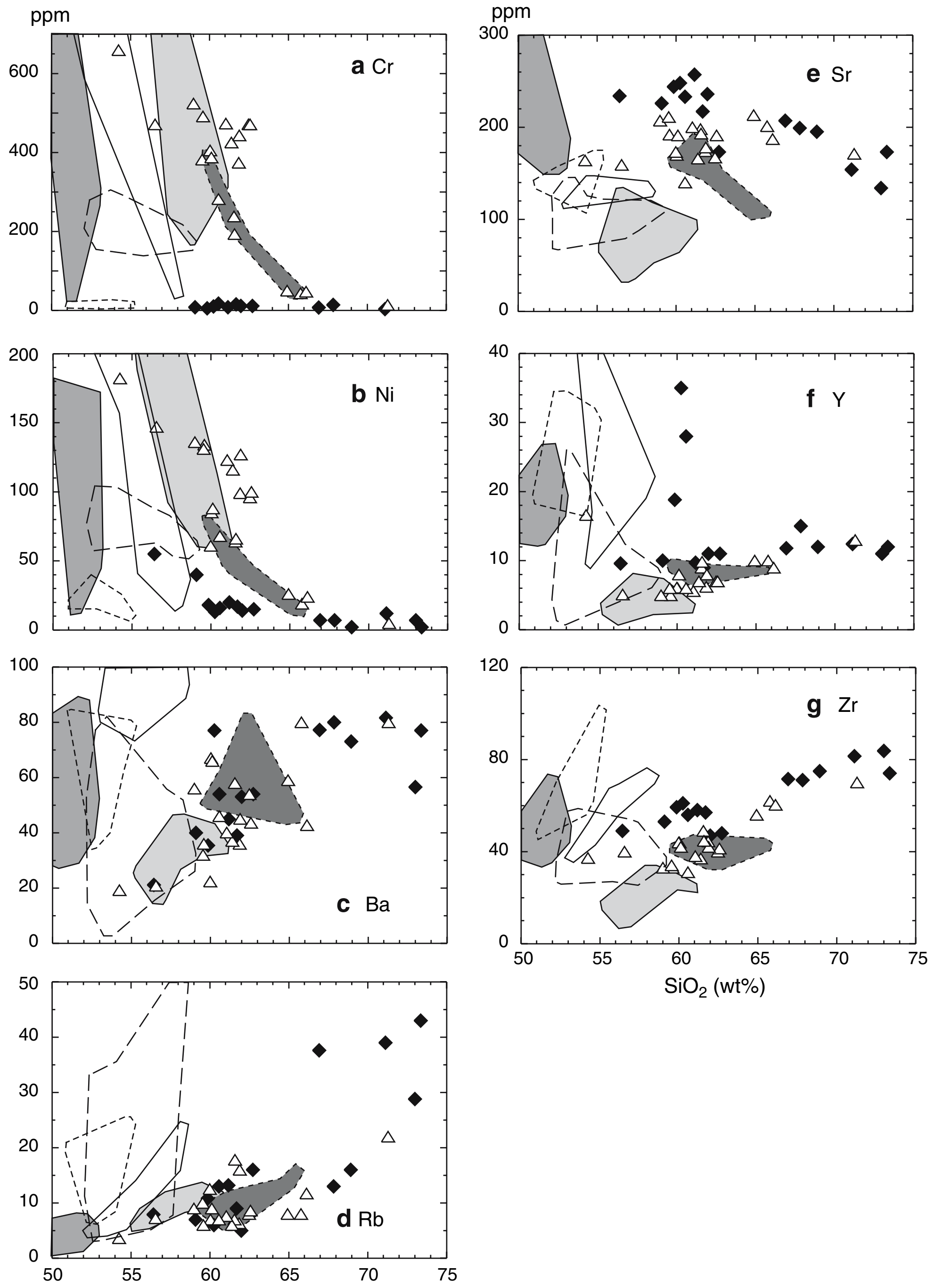

Fig. 8 Variation diagrams of selected bulk trace elements for Type A and B rocks, the early arc volcanism in the Ogasawara and Mariana regions. Symbols are same as in Fig. 7

Discussion

Difference of magma genesis conditions between Types A and B

Differences between Types A (tholeiitic) and B (boninitic) at the Site 786 are as follows: (1) Type B shows high mode and larger size of phenocrysts, and high mode of pyroxene phenocrysts. On the other hand, Type A shows low mode and small size of phenocryst, and low mode of pyroxene; (2) compared to pyroxene phenocryst composition, many Type B rocks have mafic (Mg# < 85) opx, and crystallization of temperature of Type B pyroxene phenocrysts are 50–100°C lower than that of Type A at the same Mg#; (3) many Type B rocks have calcic (>80% An content) plagioclase. These calcic placioclase phenocrysts are not observed or rare in Type A rocks; (4) Type B shows

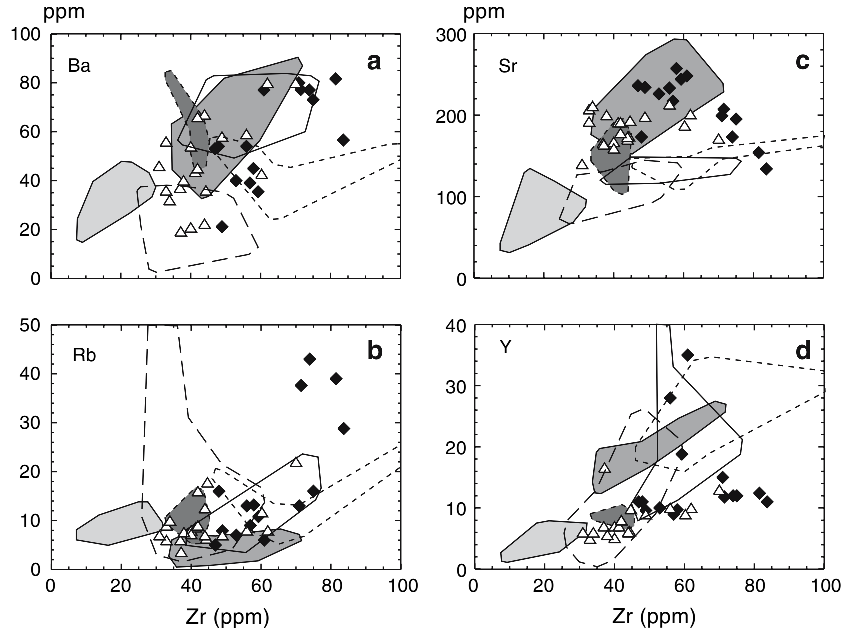

Fig. 9 Selected trace elements versus Zr variation diagrams for Type A and B rocks, the early arc volcanism in the Ogasawara and Mariana regions. Symbols are same as in Fig. 7

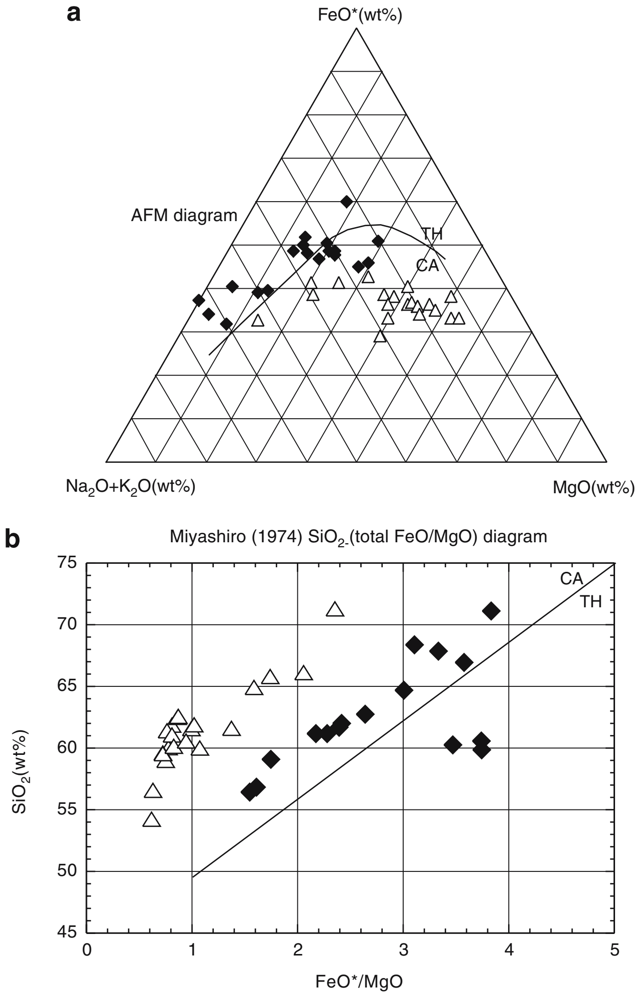

Fig. 10 AFM diagram (**a**) and Miyashiro (1974) SiO_2–(FeO*/MgO) diagram (**b**). Symbols are same as in Fig. 7

higher compatible elements concentrations than Type A in the basaltic to andesitic bulk composition; (5) both series shows low HFSE concentrations, and Type A has slightly higher HFSE content than Type B. These observations indicate that both series was active independently from each other and tholeiitic magmatism (Type A) might be not influenced by boninitic magmatism (Type B). It is considered that the tholeiite (Type A) and boninite (Type B) were produced from similar depleted mantle source. We assumed that the difference of both series was caused by difference of temperature and water condition. That is, pyroxene geothermometry indicates that the magma genesis of tholeiitic volcanism was under higher temperature condition than that of the boninitic volcanism. And calcic plagioclase, which shows high water content in the magma, was found from only Type B samples, which indicate that the boninitic volcanism was generated under water-saturated condition, and tholeiitic volcanism was generated under anhydrous condition.

Many Type B rocks show the reverse zoning in pyroxene phenocryst. Many Type A and B rocks show wide ranges of phenocrystic mineral compositions and complex frequency patterns of phenocrystic mineral composition. We assumed that complex sequence of internal magma mixing was in existence in both volcanism, i.e., mixing of primary magma and dacitic or rhyolitic magma had occurred similar to boninite generation in the Chichi-Jima (e.g., Umino and Iwano 1992). On the other hand, compositional zoning is obscure in pyroxene phenocrysts under the microscope, and chemical composition variations in pheno-

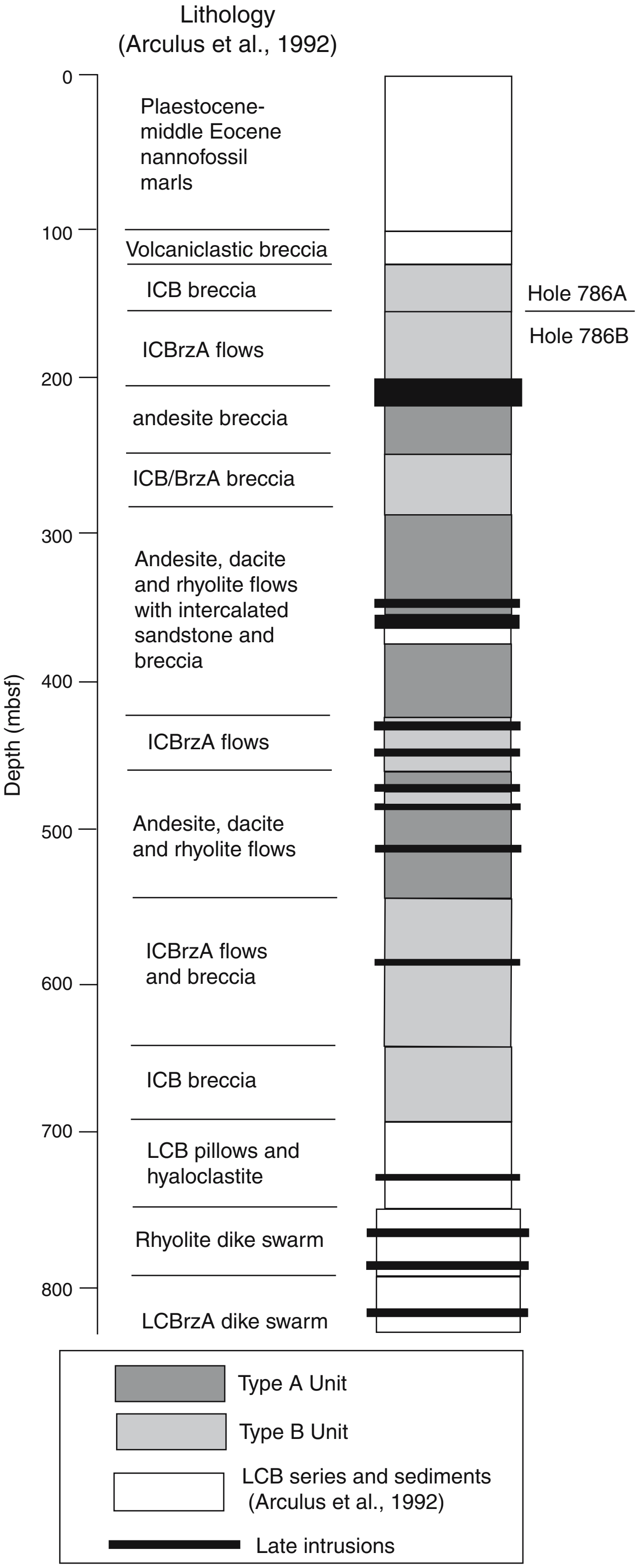

Fig. 11 Schematic lithostratigraphic section for Site 786 and distribution of unit of Type A and B. This figure is based on Pearce et al. (1992b)

crysts are simple in some Type A rocks. It is considered that this Type A rocks are associated with primitive component of Type A volcanism.

Based on this classification, tholeiite (Type A) at ODP Site 786 has the same radiometric ages as boninite (Type B), about 41 Ma in K–Ar age (Mitchell et al. 1992) and 45 Ma in Ar–Ar age (Cosca et al. 1998). These two series are interlayered in the schematic lithostratigraphic section (Fig. 11; Table 5). These complex relationships are also found in the Mariana forearc region (e.g., DSDP Leg 60 Site 458: Wood et al. 1982; Guam Island: Hickey-Vargas and Reagan 1987). Therefore, the tholeiitic volcanism in the Izu forearc region occurred at the same time as boninitic volcanism, similar to early arc volcanism in the Ogasawara region (e.g., Umino 1985), and it is generally considered that boninitic and tholeiitic volcanisms occurred closely in time and space during early arc volcanism.

Modeling of magma genesis

The model of early arc volcanism in the IBM fore-arc region (Murton et al. 1992) considered the origin of three series boninites of Arculus et al. (1992) at the Site 786. Pearce et al. (1992b) considered that three basic types of melting have been invoked to explain the recovery of a spectrum of three boninites and tholeiites: (1) in situ melting triggered by input of fluids into mantle lithosphere (e.g., Taylor and Nesbitt 1988); (2) in situ melting triggered by an input of heat into mantle lithosphere (e.g., Crawford et al. 1986) and (3) decompression melting triggered by adiabatic upwelling of depleted mantle in an extensional environment (e.g., Duncan and Green 1987). They assumed that the type of model that fits these criteria might resemble decompression–melting model.

It is assumed that the oceanic lithospheric mantle should preserve a vertical compositional zonation caused by MORB volcanism, with the most depleted peridotites lying near the top 35 km, and mantle fertility augmenting with increasing depth (Scott and Stevenson 1989). Composition of intraoceanic mantle-wedge beneath the proto-IBM arc (recent IBM forearc regions) may preserve this compositional zonation during early arc volcanism stage. Part of the depleted mantle is still able to advent melts of decompression. The uppermost part generates least melt from the most depleted lithosphere, and the lowermost part generates most melt from the least depleted lithosphere. In a single diapir, the first melt comprises pooled fractions

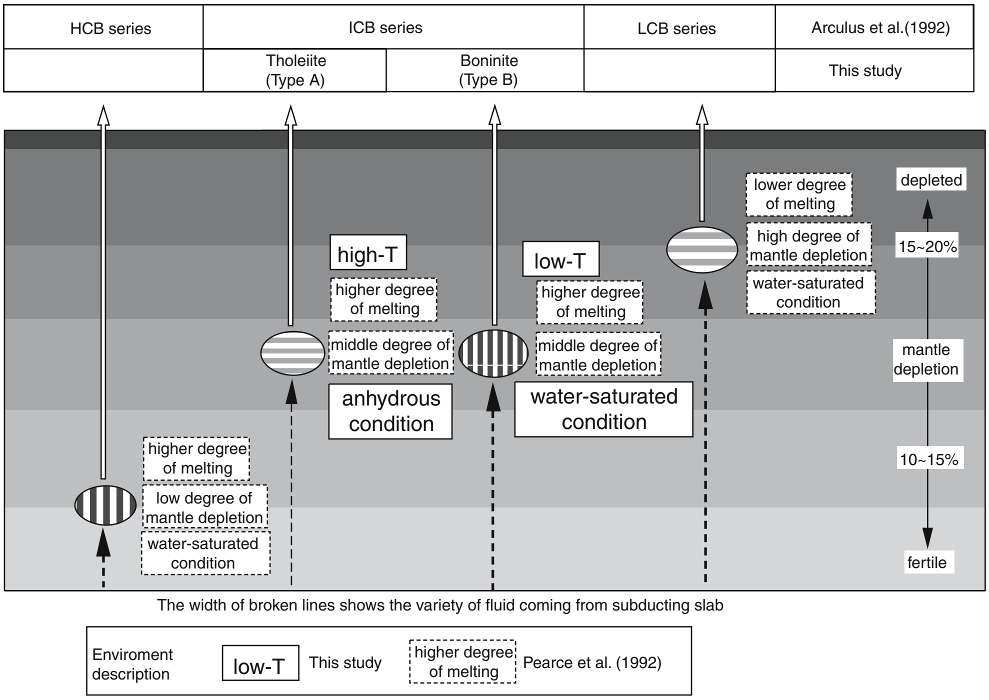

Fig. 12 Differences of magma genesis conditions between tholeiite (Type A), boninite (Type B) and other boninite series described by Pearce et al. (1992), and considered based on layered mantle model (Scott and Stevenson 1989)

from the most depleted mantle (LCB series), and the later melts to comprise pooled fractions from the least depleted mantle (HCB series) (Fig. 12).

In this study, ICB series of Murton et al. (1992) is divided into tholeiite series (Type A) and boninite series (Type B). Source materials of tholeiitic and boninitic volcanism have similar depleted composition. Boninitic magmatism was generated under low temperature and water-saturated condition. However, tholeiitic magmatism was generated under high temperature and anhydrous condition. We considered two magma genesis models that explained differences of temperature and water condition between boninite and tholeiite, and generated two series from similar depleted parent mantle. We assumed that the following two models are of same weight.

One of the possibilities is that quantity of fluid from slab dehydration is not uniformity. That is, boninitic magma was produced from low temperature zone in the wedge mantle with excessive supply of fluid from slab dehydration. On the other hand, tholeiitic magma was produced from high temperature zone in the wedge mantle with short supply of fluid from slab dehydration (independent genesis model, Fig. 13a).

The other possibility is zoned mantle diapir (Zoned diapir model, Fig. 13b). This model was proposed by Tamura (1994) who studied the Shirahama volcanic complex in the Izu Peninsula. This model is that the H_2O-rich mantle diapir had risen in wedge mantle which is hot and dry, mantle diapir had been heated and dehydrated by wedge mantle during rising in this region, and had separated two compositions, hydrous, cooler core and anhydrous, hotter rim. This mantle diapir would generate tholeiitic basalt from its hot anhydrous rim and boninite from its hydrous cooler interior.

Conclusions

Volcanic rocks recovered from ODP Leg 125 Site 786 in the Izu forearc region are divided into the tholeiite and boninite series based on petrographical and petrological properties. Tholeiite series rocks are characterized by low mode of phenocrysts, high ratio of pl in phenocrysts, small size of phenocrysts and glassy groundmass. In contrast, boninite series rocks are characterized by high mode of phenocrysts, high ratio of pyroxene in phenocrysts, large size of phenocrysts and relatively non-glassy groundmass. Both types have different mineral compositions; pyroxene phenocrysts in the tholeiites show narrow compositional ranges and high crystallization temperatures; those in the boninites show wide compositional range, compositionally complex distribution patterns and low crystallization temperatures.

The tholeiite and boninite series have same source materials, depleted mantle because of resemblance of bulk HFSE concentrations and chondrite–normalized patterns. The origin of producing different series

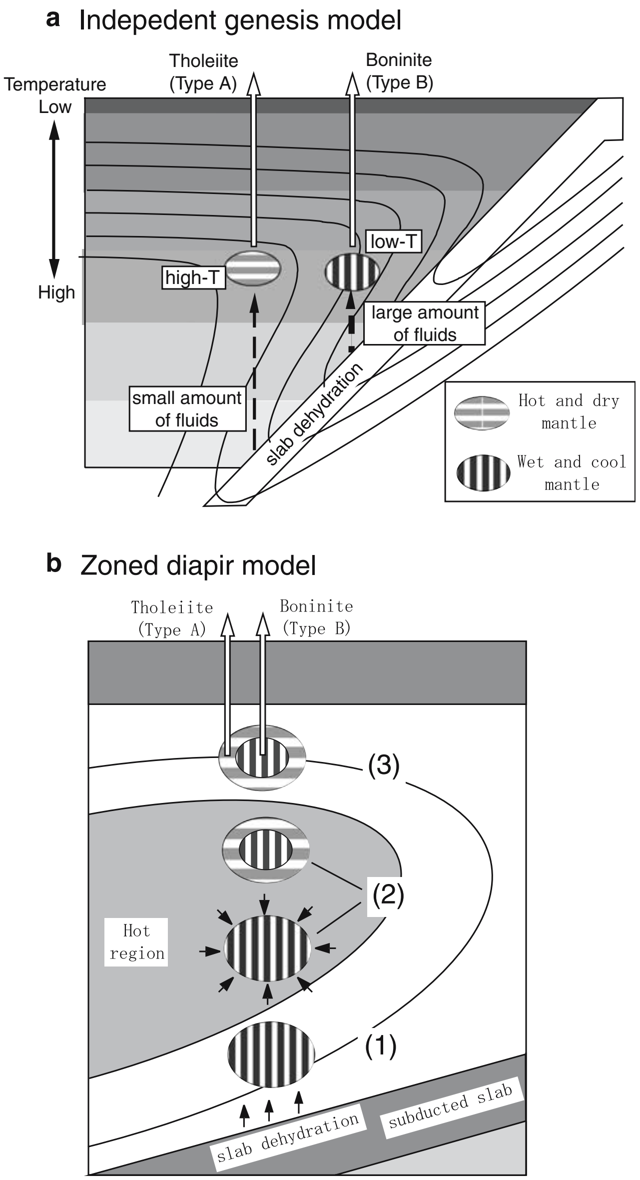

Fig. 13 **a** Independent genesis model: (1) Boninitic magma was generated under fluid-rich and low-temperature condition in the outer wedge mantle, and (2) tholeiitic magna was generated under fluid-poor and high-temperature condition in the inner wedge mantle which is same as depletion and depth of the parent mantle of boninite. **b** Zoned diapir model: The model for boninic and tholeiitic magma genesis by zoned mantle diapir model (Tamura 1994). (1) The mantle diapir had been produced above the subducting slab. This mantle diapir was enriched H_2O which was from dehydration of subducting slab. (2) The mantle diapir had risen in wedge mantle which is hot and dry. These had been heated and dehydrated by wedge mantle during rising in this region. Through this process, mantle diapir had separated two composition, hydrous, cooler core and anhydrous, hotter rim. (3) When zoned mantle diapir had arrived at upper mantle, mantle diapir would generate tholeiite from its hot anhydrous rim and boninite from its H_2O-enriched cooler interior, and these two magma series had erupted

magma is caused by difference of water condition; boninite series was produced under water-saturated condition and tholeiite series were produced under anhydrous condition.

Both series rocks are interlayered in the section, and tholeiite at Site 786 has the same radiometric ages as boninite. Therefore, the tholeiitic volcanism in the Izu forearc region occurred at the same time as boninitic volcanism.

Acknowledgements We are rate to Dr. Susumu Umino, Dr. Yasuhiko Ohara, and Dr. Hidekazu Taniguchi for discussions. We would like to thank Dr. Graciano P. Yumul Jr., Dr. Daniel Curewitz, and Dr. Hoang Nguyen for detailed comments on the manuscript.

References

Arculus RJ, Pearce JA, Multon BJ, van der Laan SR (1992) Igneous stratigraphy and major-element geochemistry of holes 786A and 786B. In: Fryer P, Pearce JA, Stolling LB et al (eds.) Proc ODP Sci Res 125:143–168

Bence SE, Albee AL (1968) Empirical correction factors for the electron microanalysis of silicates and oxides. J Geol 76:382–402

Cosca MA, Arculus RJ, Pearce JA, Mitchell JB (1998) ^{40}Ar/^{39}Ar and K–Ar geochronological age constraints for the inception and early evolution of the Izu–Bonin–Mariana arc system. Island Arc 7:579–595

Crawford AJ, Beccalvua L, Serri G, Dostal J (1986) Petrology, geochemistry and tectonic implications of volcanic dredged from the intersection of the Yap and Mariana trenches. Earth Planet Sci Lett 80:265–280

Crawford AJ, Falloon TJ, Green DH (1989) Classification, petrogenesis and tectonic setting of boninites. In: Crawford AJ (ed) Boninite and related rocks. Unwin Hyman, London, pp 1–49

Dancan RA, Green DH (1987) The genesis of refractory melts in formation of the oceanic crust. Contrib Mineral Petrol 96:326–342

Haraguchi S, Ishii T, Kimura J-I, Ohara Y (2003) Formation of tonalite from basaltic magma at the Komahashi-Daini Seamount, northern Kyushu-Palau Ridge in the Philippine Sea, and Growth of Izu-Ogasawara (Bonin)-Mariana arc crust. Contrib Mineral Petrol 145:151–168

Hickey-Vargas R (1989) Boninites and tholeiites from DSDP site 458, Mariana Forearc. In: Crawford AJ (ed) Boninites and related rocks. Unwin Hyman, London, pp 339–356

Hickey-Vargas R, Reagan MK (1987) Temporal variations of isotope and rare earth element abundance from Guam: imprecations for the evolution of the Mariana arc. Contrib Mineral Petrol 97:497–508

Honza E, Fujioka K (2004) Formations of arcs and backarc basins inferred from the tectonic evolutions of Southeast Asia since the Late Cretaceous. Tectonophysics 384:23–53

Ishii T (1975) The relations between temperature and composition of pigeonite in some lavas and their application to geothermometry. Mineral J 8:48–57

Ishii T (1981) Pyroxene geothermometry of basalts and an andesite from the Palau-Kyushu and West Mariana ridges. In: Kroenke L, Scott R et al (eds) Deep sea drilling project leg 59. Init Rept DSDP, vol 59, pp 693–718

Kuno H, (1953) Formation of calderas and magmatic evolution. Trans Am Geophys Union 34:267–280

Maehara K, Maeda J (2004) Evidence for high-Ca boninite magmatism from Paleogene primitive low-K tholeiite, Mukoojima, Hahajima Island group, southern Bonin (Ogasawara) forearc, Japan. Island Arc 13:452–465

Mitchell JG, Peate DW, Murton BJ, Pearce JA, Arculus RJ, van der Laan SR (1992) K–Ar dating of samples from sites 782 and 786 (Leg 125): the Izu–Bonin forearc region. In: Fryer P, Pearce JA, Stolling LB et al (eds) Proc ODP Sci Res 125:203–210

Miyashiro A (1974) Volcanic rock series in island arcs and active continental margins. Am J Sci 274:321–355

Murton BJ, Peate DW, Arculus RJ, Pearce JA, van der Laan SR (1992) Trace-element geochemistry of volcanic rocks from Site 786: the Izu–Bonin forearc. In: Fryer P, Pearce JA, Stolling LB et al (eds) Proc ODP Sci Res 125:211–235

Nakamura Y, Kushiro I (1970) Compositional relations of coexisting orthopyroxene, pigeonite, and augite in a tholeiitic andesite from Hakone Volcano. Contrib Mineral Petrol 26:265–275

Pearce JA, Thirlwall MF, Ingram G, Murton BL, Arculus RJ, van der Laan SR (1992a) Isotopic evidence for the origin of boninites and related rocks drilled in the Izu–Bonin (Ogasawara) forearc, Leg 125. In: Fryer P, Pearce JA, Stolling LB et al (eds) Proc ODP Sci Res 125:237–261

Pearce JA, van der Laan SR, Arculus RJ, Murton BJ, Ishii T, Peate DW, Parkinson IJ (1992b) Boninite and harzburgite from Leg 125 (Bonin–Mariana forearc): a case study of magma genesis during the initial stages of subduction. In: Fryer P, Pearce JA, Stolling LB et al (eds) Proc ODP Sci Res 125:623–659

Reagan M, Meijer A (1984) Geology and geochemistry of early arc-volcanic rocks from Guam. Geol Soc Am Bull 95:701–713

Scott DR, Stevenson DJ (1989) A self-consistent model of melting, magma migration and buoyancy driven circulation beneath Mid-Ocean Ridges. J Geophys Res 94:2973–2988

Tamura Y (1994) Cenesis of island arc magmas by mantle-derived bimodal mgamatism: evidence from the Shirhama group, Japan. J Petrol 35:619–645

Tatsumi Y, Maruyama S (1989) Boninites and high-Mg andesites: tectonics and petrogenesis. In: Crawford AJ (ed) Boninites and related rocks. Unwin Hyman, London, pp 50–71

Taylor RN, Nesbitt RW (1988) Light rare earth enrichment of supra-subduction zone: evidence from the Troodos ophiolite, Cyprus. Geology 16:448–451

Taylor RN, Lapierre H, Vidal P, Nesbitt RW, Croudace IW (1992) Igneous geochemistry and petrogenesis of the Izu–Bonin forearc basin. In: Taylor B, Fujioka K et al (eds) Proc ODP Sci Res 126:405–430

Taylor RN, Nesbitt RW, Vidal P, Harmon RS, Auvray R, Croudace TW (1994) Mineralogy, chemistry, and genesis of the boninite series volcanics, Chichijima, Bonin Islands, Japan. J Petrol 35:577–617

Umino S (1985) Volcanic geology of Chichijima the Bonin Islands (Ogasawara Islands). J Geol Soc Jpn 91:505–523

Umino S (1986) Magma mixing in boninite sequence of Chichijima, Bonin Islands. J Volcanal Geotherm Res 29:125–157

Umino S, Iwano M (1992) Origin of porphyritic boninite—destruction of mushy layer by fountains in magma chamber. J Volcanol Soc Jpn 37:183–203

Wells PRA (1977) Pyroxene thermometry in simpled and complex systems. Contrib Mineral Petrol 62:129–139

Wood BL, Banno S (1973) Garnet–orthopyroxene and orthopyroxene–clinopyroxene relationships in simple and complex systems. Comtrib Mineral Petrol 42:109–124

Wood DA, Marsh MG, Tarney J-L, Fryer P, Treuil M (1982) Geochemistry of igneous rocks recovered from a transect across the Mariana Trough, Arc, Fore-arc, and Trench, Site 453 through 461. Deep sea drilling project leg 60. In: Hussong DM, Uyeda S et al (eds) Init Rept DSDP 60:611–645